Research on Stable, High-Efficiency Amorphous Silicon Multijunction Modules

Final Subcontract Report
1 May 1990 – 30 June 1993

R. R. Arya, M. Bennett, L. Chen,
B. Fieselmann, Y. Li, N. Maley,
J. Newton, R. Podlesny, L. Yang
Solarex Thin Film Division
Newtown, Pennsylvania

NREL

Research on Stable, High-Efficiency, Amorphous Silicon Multijunction Modules

Final Subcontract Report
1 May 1990 – 30 June 1993

R. R. Arya, M. Bennett, L. Chen,
B. Fieselmann, Y. Li, N. Maley,
J. Newton, R. Podlesny, L. Yang
Solarex Thin Film Division
Newtown, Pennsylvania

NREL technical monitor: W. Luft

NREL

NOTICE

PREFACE

The work described in this report is the culmination of research performed under subcontract #ZM-0-19033-1. The work was performed in three phases which covers the period May 1, 1990 through June 30, 1993. The details of Phase I and Phase II efforts under this subcontract were published under SERI/TP-214-4271, SERI/TP-214-4405, NREL/TP-451-4720, and NREL/TP-411-4995.

EXECUTIVE SUMMARY

Goal: The primary goal of the phase III effort is to demonstrate a multijunction module with a "stabilized" efficiency (600 hours, 50°C, AM 1.5) of 12%.

Approach: Triple-junction modules employing a-Si:H and its alloys were used in conjunction with improved front tin oxide and zinc oxide to meet the program goals.

Introduction

This is a final report of a 3-year effort which covers the period May 1, 1990 through June 30, 1993. During this period major improvements were achieved in the stabilized conversion efficiency of triple-junction modules. This has resulted in the demonstration of triple-junction initial conversion efficiency of 11.3% and stabilized conversion efficiency of ~ 9%.

Significant advances were made in the deposition of a-Si:H intrinsic layers which led to higher open-circuit voltage and improved stability. Thin microcrystalline n-layers were developed and scaled-up for the recombination junctions in triple-junction modules which have resulted in higher open-circuit voltage and fill-factor. These improvements have resulted in the demonstration of a-Si/a-Si/a-SiGe triple-junction modules with initial conversion efficiency as high as 11.35% and "stabilized" efficiency of about 9%.

Task I: Semiconductor Materials and Device Research

The development of low-temperature, H-diluted a-Si:H intrinsic layers have shown remarkable improvement in the performance and stability of single-junction solar cells. Optimization of H-dilution has led to i-layer material which shows lower concentrations of "di-hydride" bonding in the IR spectra. The p-i-n devices fabricated under low-temperature, H-dilution conditions exhibit V_{oc}'s much higher than expected from the increase in bandgap of the i-layer material alone. Moreover, the behavior of these devices after light-soaking is different - the efficiency saturates in short times (a few hundred hours) compared to 1000 hours or more for devices prepared at high temperature and without H-dilution. We have also developed very thin (~10 nm thick) microcrystalline n-layers for the 'recombination junctions'. This has led to increases in V_{oc}, FF and J_{sc}.

Task II: Non-Semiconductor Materials Research

Several approaches were undertaken to improve the front contact and the rear contact of triple-junction modules. Optimization of deposition parameters for textured tin oxide has resulted in increases of 3-4% in the short-circuit current of the devices. Development of ZnO front contact by atmospheric pressure chemical vapor deposition (APCVD) was not very successful. ZnO films had problems with uniformity and control of surface morphology (texture). We have started exploring deposition of textured ZnO by low pressure chemical vapor deposition (LPCVD) and have achieved excellent uniformity and sheet resistance. Devices on LPCVD deposited ZnO have not yet resulted in the desired improvements in conversion efficiency. Optimization of the ZnO/Ag rear contact has shown moderate improvement in the long-wavelength response of single-junction devices.

Task III: Module Development

The developments in Task I have been scaled-up and have resulted in improved performance of a-Si/a-Si/a-SiGe triple-junction modules. The improvements in textured tin oxide have not yet been incorporated in large area modules. These improvements have resulted in a dual-bandgap, triple-junction module with initial conversion efficiency of 11.35%. The "stabilized" conversion efficiency was 9.15% after > 600 hours of light-soaking under AM 1.5 illumination at 50°C. We expect to increase the initial conversion efficiency to over 12% and the stabilized conversion efficiency to over 10% by incorporating the advances made in Task II, both in the front contact and in the rear contact of the modules.

TABLE OF CONTENTS

LIST OF TABLES

1.0 INTRODUCTION

Significant advances were made in the deposition of intrinsic amorphous silicon which resulted in higher open-circuit voltage and improved stability. This development was mainly due to Deposition of a-Si:H from a mixture of silane and hydrogen at low substrate temperatures. The resultant a-Si:H films show lower concentrations of "di-hydride bonding". The gains in open-circuit voltage of single-junction solar cells is larger than what would be expected from widening of bandgap due to lower substrate temperatures. It is speculated that at lower temperatures the p/i interface is also modified which contributes to the higher open-circuit voltages. The single-junction devices show a very different behavior on light-soaking - the light-induced degradation saturates after a few hundred hours of light-soaking. We also successfully developed thin micro-crystalline n-layers for the tunnel junctions in triple-junction modules. This has resulted in improvements in V_{oc}, F.F and J_{sc} of the middle cell in triple-junction cells.

Development of textured ZnO by atmospheric chemical vapor deposition (APCVD) was not successful. Particularly, reproducibility, uniformity and desired texture were difficult to maintain. The few times that we did succeed in such films we did fabricate small area solar cells with improved currents. In the latter part of the program we switched to the development of textured ZnO by low-pressure chemical vapor deposition (LPCVD). The initial results are encouraging in that films with similar optical and electrical properties can be reproducibly produced. Optimization of the ZnO/Ag rear contact showed moderate improvement in the long-wavelength response of single-junction devices. These improvements have not yet been incorporated into large-area modules.

We successfully incorporated the developments in intrinsic a-Si:H and in microcrystalline n-layers to large-area triple-junction modules. Large area (> 900 cm2) triple-junction modules were fabricated with the device structure:

<div align="center">a-Si:H / a-Si:H / a-SiGe:H</div>

Laser scribing was optimized to result in over 98% area utilization in triple-junction modules. The effect of shunts on the initial performance and on the degradation was also quantified. Initial studies indicate that 3%-5% degradation in modules is not due to the semiconductor layers but is due to shunts. The origin of shunts is a difficult problem and investigations are ongoing.

2.0 Task I: SEMICONDUCTOR MATERIALS RESEARCH

2.1 Introduction

Semiconductor materials research includes development of a-Si:H intrinsic layers, a-Si:H alloys intrinsic layers, microcrystalline doped layers, and modeling of light-inducted degradation of single-junction solar cells. The most significant results include: (i) The development of a-Si:H i-layer material at low substrate temperature and high hydrogen dilution. This has resulted in p-i-n devices with initial V_{oc}'s > 1.0 V and improved stability. The stability is not only improved in its magnitude but shows definite stabilization after a few hundred hours of light soaking. (ii) The development and scale-up of 'thin' microcrystalline n-layers used at the tunnel junction(s) of multijunction solar cells and modules. This has improved the V_{oc}, the J_{sc} and the F.F of multijunction solar cells and modules.

2.2 Improved a-Si:H Cells Made from H_2-diluted SiH_4 at Low Temperatures

The a-Si:H i-layer material has been traditionally made at Solarex by d.c. glow discharge of pure SiH_4 at ~260°C substrate temperature. However, in investigating the influence of deposition temperature on stability we noticed that the open-circuit voltage of cells was increasing faster than the optical gap and that as the deposition temperature was lowered substantial increases in open-circuit voltage could be obtained. Moreover, when H_2-dilution was used in conjunction with lower substrate temperature, the devices even showed improved stability compared to those made at high temperature.

The structural and photoelectronic properties of the materials made with H_2-dilution at low temperatures have been investigated and compared to those of the traditional material.
Figure 2.1 shows the optical bandgap (defined as energy at which absorption is 2×10^3 cm^{-1}, measured by Photo-Thermal deflection spectroscopy) as the deposition temperature is lowered for films deposited from SiH_4 and from SiH_4 diluted in H_2. The gap changes by about 0.20 eV over the entire range of deposition temperature whether or not the SiH_4 is diluted in H_2 during the deposition. The effect of H_2 dilution can be seen more clearly in the IR spectra of low-temperature films in **Figure 2.2** where the H_2 dilution varies from 2:1 to 10:1. As the degree of dilution increases, the peaks at 2090 cm^{-1} and 640 cm^{-1} grow smaller, indicating that the total hydrogen content of the films is decreasing. Although dilution has improved the structure of the material as indicated by the spectra of **Figure. 2.2**, the width of the peak at 2000 cm^{-1} is still broader than it is in films made at 270°C without H_2 dilution. Although these films were not light soaked, the stability of cells can usually be related

in an inversely proportional way to the size of the peak at 2090 cm^{-1} in the IR spectrum of the material comprising their i-layers [1].
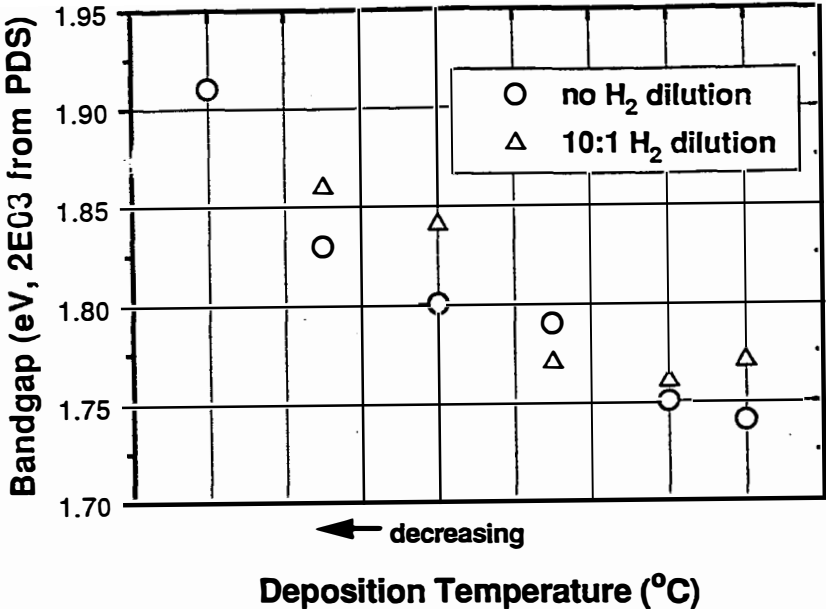
Figure 2.1 Bandgap vs. Deposition Temperature for a-Si:H films made with and without dilution.
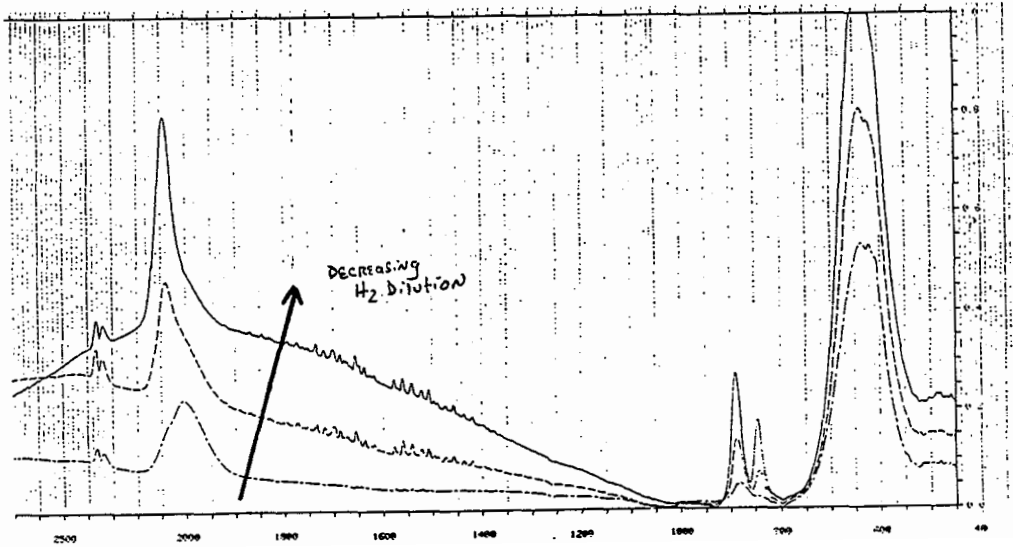
Figure 2.2 Effect of decreasing H$_2$-dilution of IR spectra of a-Si:H films made at a low temperature.

3

Cells were made incorporating the i-layers described above into single-junction p-i-n devices. **Figure 2.3** shows the dependence of V_{oc} and the optical bandgap, $E_{g'opt}$ on deposition temperature. Obviously the open-circuit voltage depends on more than the optical bandgap. This result is true for cells made in either a single- or multi-chamber deposition system. **Table 2.1** compares the cell characteristics for a "standard cell", which has its i-layer deposited at 270°C from SiH_4 to the characteristics of a cell having its i-layer deposited at a lower temperature with optimized materials properties and structure. There is a substantial gain in V_{oc} and a small loss in J_{sc} resulting a large (6%) overall gain in efficiency. **Figure 2.4** compares the quantum efficiency for the two devices, showing that the loss in current is a consequence of the slight increase in bandgap due to the low temperature of deposition. In fact, the differences shown in **Table 2.1** and **Figure 2.4** are due to the lowering of the deposition temperature.

Perhaps more significant than the improvement in their open-circuit voltages, the cells made at low temperature with H_2-dilution show improved stability over the traditional cells with the same thickness. Cells made under standard conditions of no H_2 dilution at 270°C show a linear decrease in efficiency with the log of exposure time [2]. However, cells made at lower temperatures under optimal conditions show a qualitatively different functional dependence of efficiency on exposure time. The comparison is shown in **Figure 2.5** where it can be seen that cells made at a low temperature under H_2 dilution show a slowing of the rate of degradation and approach saturation. The cells whose performance over time is shown in **Figure 2.5** do not have a SiC p-i interface layer. If these cells are provided with an optimized SiC p-i interface layer and hence have a considerably higher initial efficiency, they do not suffer any greater light-induced degradation as a result of the interface layer. Cells deposited at low temperature with H_2-dilution also show not only a higher initial V_{oc}, but also improved stability in their open-circuit voltage. Formerly, the loss in V_{oc} was about 5% in 1000 hours. The low-temperature H_2-diluted devices, even though they have higher open-circuit voltage, decay by only about 2% or 3%. We also investigated the effect of the amount of H_2-dilution on stability. We found that the effect of dilution on the IR spectra of films noted in **Figure 2.2** is reflected in the curves of efficiency vs. time shown in **Figure 2.6**. As the IR peaks at 2090 cm^{-1} decreases of the films with increasing dilution, so does the stability of the cells improve as the amount of dilution used in growing the i-layer increases.

4
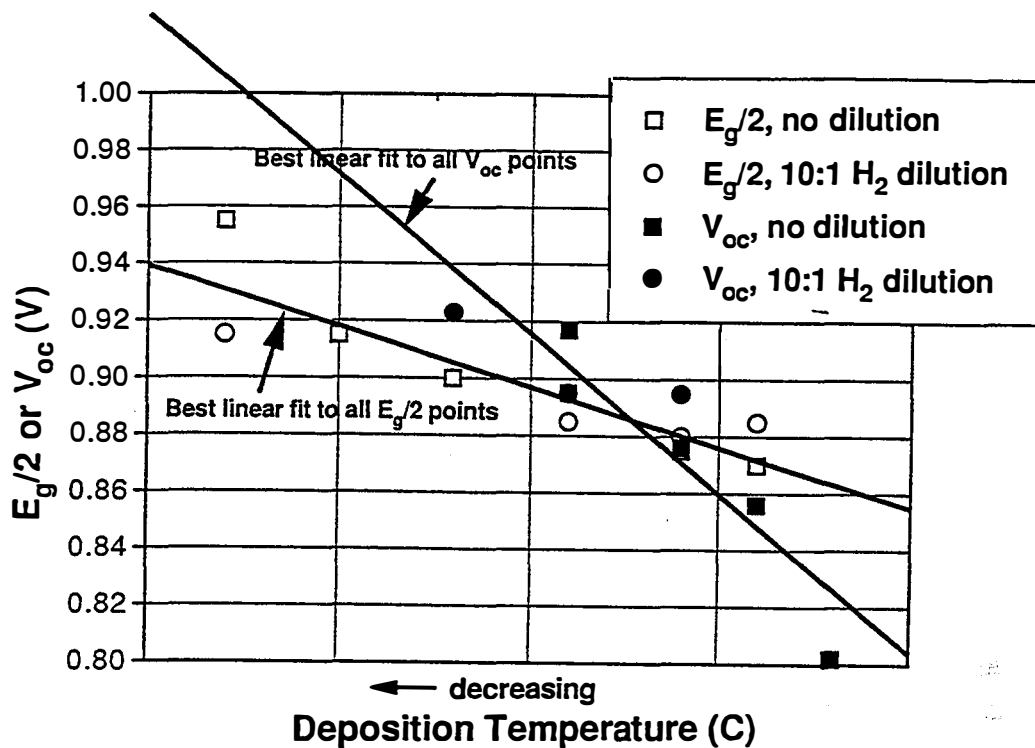
Figure 2.3 Eg/2 and V_{oc} for films and cells made at different deposition temperatures with and without H_2-dilution.

Table 2.1 A comparison of our best cells made at low substrate temperature and at 270°C (before light soaking).

Deposition Condition	V_{oc} (V)	Fill Factor	Jsc (mA/cm^2)	Eff. (%)
Low temp, optimized deposition	0.925	0.705	13.9	9.06
Standard deposition 270°C	0.864	0.698	14.2	8.56
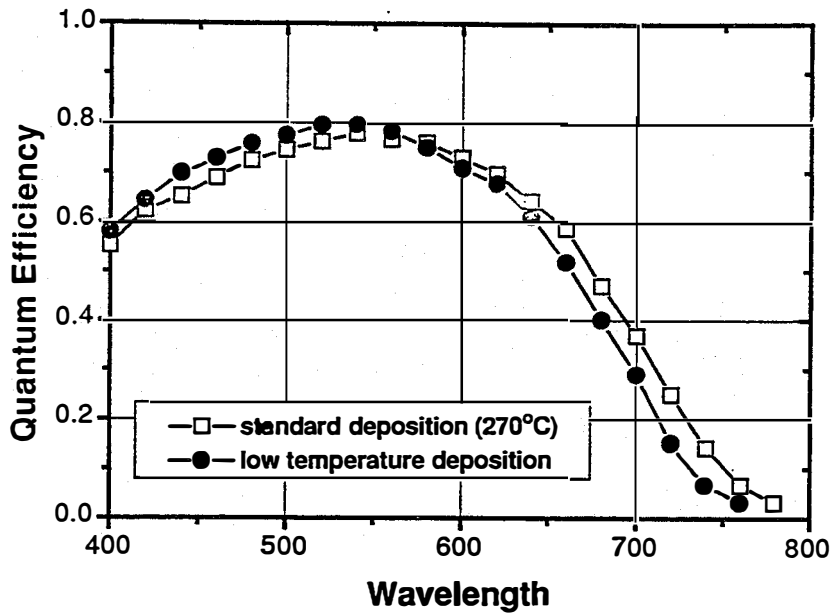
Figure 2.4 Quantum efficiency of cells made under standard conditions and at low temperature with H_2-dilution.
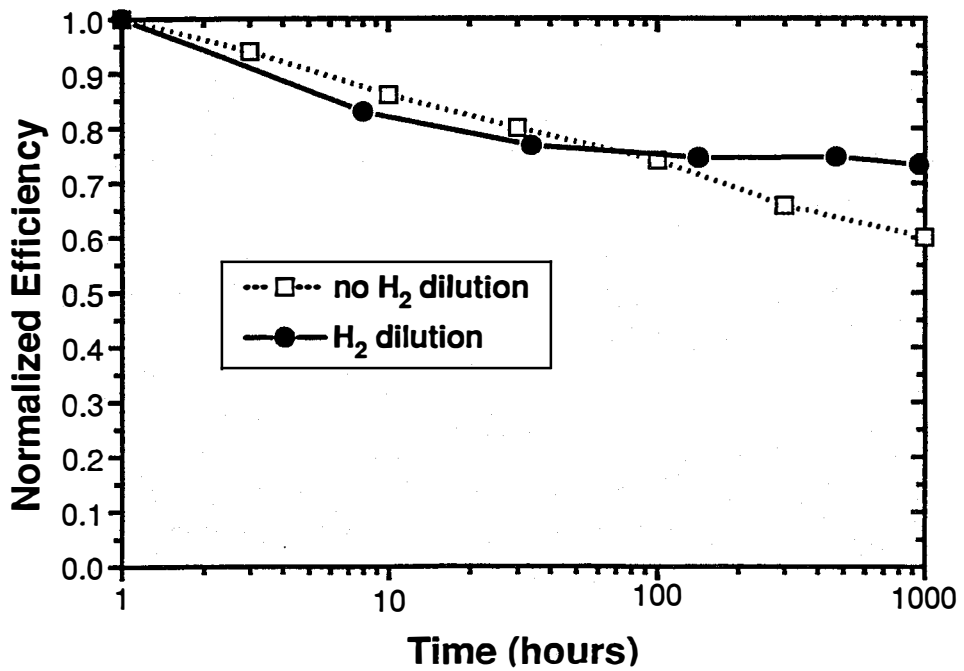
Figure 2.5 Normalized efficiency of cells made high temperature without H_2-dilution and at low temperature with H_2-dilution.
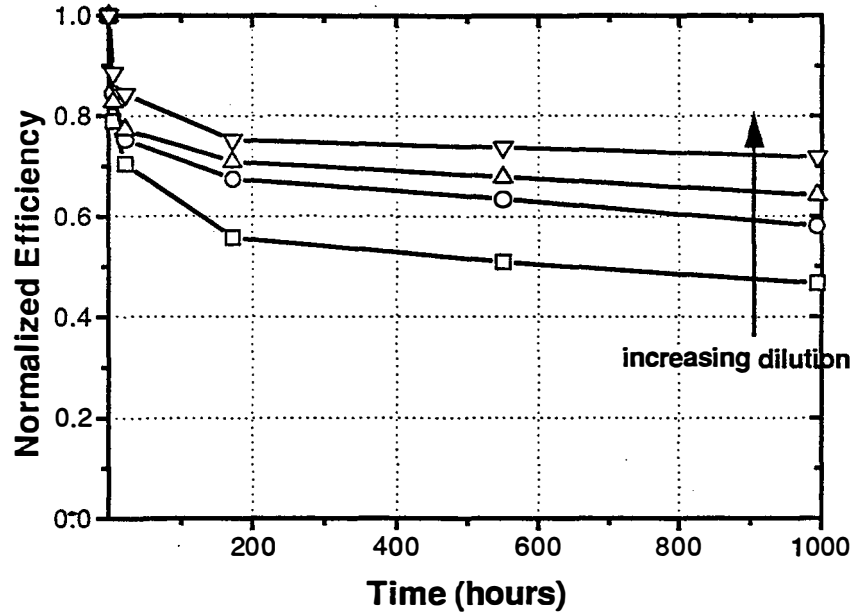
Figure 2.6 The effect of increasing H_2-dilution on the change in normalized efficiency as a function of degradation time for a-Si:H p-i-n cells.

Dark I-V measurements were made on a few cells. These showed diode factors as high as 1.98. compared to about 1.7 which is what we typically measure on cells deposited at high temperature. Furthermore, there is less degradation of the diode characteristic with light soaking. Formerly the diode factor would increase from about 1.7 to about 2.35 with light soaking. The cells deposited at low temperature show a much smaller increase, typically from 1.9 to about 2.2. At a given deposition temperature, the rate of degradation apparently increases with decreasing ratio of H_2-dilution.

Measurements show that the ambipolar diffusion length, measured by steady-state photograting technique (by SSPG), photoconductivity and dark conductivity (coplanar measurement), and Urbach energy and subgap absorption (by PDS) do not depend on the presence or absence of H_2-dilution and are at best very weak functions of temperature. The only significant observed differences, aside from the slight change in bandgap, were in the IR spectra which were very dependent on the degree of dilution at low deposition temperatures. *Thus, given the close similarity between the films grown without H_2-dilution at 270°C and those grown with H_2-dilution at low temperature, the difference between the cells made under the two conditions is surprising.* The increase in voltage can be only partially explained by the increase in bandgap. The remainder of the increase must be related to differences in transport properties. This may reflect a difference in the recombination processes occurring throughout the i-layer and/or at the p-i interface.

7

As evidence for a possible difference in transport, we cite the difference in the diode quality factor, which was as high as 1.98 in the low temperature, H_2-diluted devices. In cells made at high temperature the diode factor is typically 1.7 - 1.75 and never as high as 1.9. Given our inability to distinguish the low temperature H_2-diluted films from the high temperature films grown without dilution on the basis of bulk transport properties, we suspect that if there is an improvement in transport which is responsible for in part for the increase in V_{oc} in cells, it is occurring primarily in the p-i interface region.

The improvement in stability is a result of optimization of deposition parameters and cell structure. At low temperature, the film property that we associate with stability, namely, IR spectra, showed significant improvement as dilution was increased. In the past, we have always considered the Staebler-Wronski effect to be a bulk effect, since, as the i-layer thickness goes to zero, the degradation goes to zero, with a nearly linear dependence. While under certain circumstances the p-i interface could be shown to worsen in stability, this was usually a small effect compared to that of thickness. Without detailed kinetic studies it is difficult to analyze what is happening. However, it is reasonable to hypothesize that the same changes are responsible for both the improved V_{oc} and stability. Thus we hypothesize that the improvement in stability is also related to improvements in transport at the interface. More detailed kinetic studies are underway.

2.3 Microcrystalline Tunnel Junction

Doped microcrystalline Si (μc-Si) represents a very attractive alternative for a-Si:H based solar cells not only because of its much improved electrical and optical properties but also because of its compatibility with the low-temperature PECVD process. However, except for very few reported successes, [3-5] microcrystalline Si so far has not been widely used in a-Si:H solar cells, at least for commercial applications. The main difficulties are perhaps in making extremely thin layers of μc-Si (<100 Å), which is necessary in order to reduce the optical loss, and in alloying with carbon for raising the optical bandgap. We emphasized those issues related to the growth of ultra-thin microcrystalline materials which are of special concern to the application in a-Si:H based solar cells. Furthermore, we demonstrated the use of microcrystalline Si in multijunction solar cells which has resulted in significant improvement in all aspects of device performance [6].

A large volume of literature has been devoted to the growth and properties of μc-Si [7]. However, much of it has been focused on the bulk properties which are known to be much different from those of extremely thin layers made under the same "microcrystalline" condition [8-10]. Therefore, it has little relevance to the application of μc-Si in solar cells where only ultra-thin

layers are used. **Figure 2.7** shows the thickness dependencies of dark conductivity and activation energy for films made under a typical "microcrystalline" p-layer condition. It is clearly illustrated in the figure that the film properties change dramatically when thickness is below ~1000 Å. This is not terribly surprising because it is well known that nucleation is critical in forming crystalline grains on a heterogeneous substrate. Therefore, it is easy to imagine that the properties of those films made under "microcrystalline" conditions are also strongly substrate dependent, especially for ultra-thin layers. Indeed, it has been reported that the formation of microcrystalline Si on an a-Si:H substrate is easier than on the conducting SnO_2 substrate used as the transparent front contact in the solar cell [10]. In addition to the material type, whether the substrate is conducting or insulating apparently also influences the initial nucleation of μc-Si, at least in a d.c. plasma. This makes it very difficult to characterize the exact material to be incorporated in the device because conventional material characterizations such as the conductivity measurement and Raman spectroscopy are usually made on samples deposited on different substrates. Therefore, the materials issues central to the application of μc-Si doped layers in a-Si:H based solar cells are: (1) to find means to characterize the ultra-thin layers exactly as or similar to those incorporated in the devices, and (2) to develop proper methods to promote fast nucleation of μc-Si on desired substrates. While the device itself is the ultimate test of the material properties, we show in the following that useful information can be obtained from film characterization when special care is taken with regard to the film thickness and substrate.
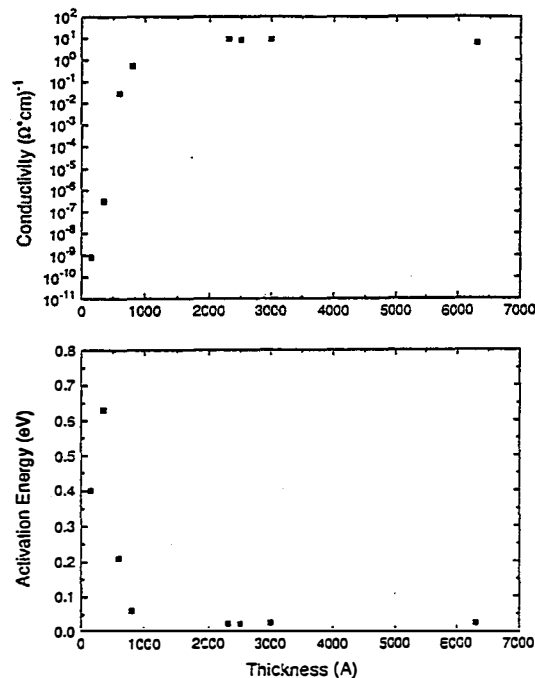
Figure 2.7 Thickness dependences of dark conductivity and activation energy of films made under a typical p-type "microcrystalline" condition.

9

Raman spectroscopy is a very sensitive tool to distinguish microcrystalline materials from amorphous. However, for ultra-thin films on the order of 100 Å it is essential that the samples are deposited on metal or other substrates which generate very low scattering signal in the spectral range of interest. Quartz substrates usually have an excessive photoluminescence background that washes out the Raman signal from the subject film. Likewise, when the ultra-thin layer is deposited on a relatively thick a-Si:H layer the Raman signal of the top layer can be dominated by that due to a-Si:H underneath. Therefore, to study the properties of a "micro-crystalline" ultra-thin layer on a-Si:H using Raman spectroscopy it is best to first deposit an ultra-thin a-Si:H layer of ~50 Å on a metal substrate and then deposit the "microcrystalline" over-layer. The Raman system we use is a Spex triple-mate monochrometer equipped with an optical multichannel analyzer (OMA) which is cooled at about -15°C. An Ar+ ion laser at typically 514.5 nm is used as the excitation light and the input power level is kept at ~100 mW to avoid over-heating the sample. Using an OMA significantly increases the measurement efficiency as compared to using a photo-multiplier tube (PMT) and scanning the wavelength range. A typical Raman spectrum of an a-Si:H thin layer thus takes only about 10 min. **Figure 2.8** shows the Raman spectra of several n-type Si films made under a "microcrystalline" condition on various substrates. The nominal film thickness of all films is ~100 Å except the one for Curve (a) which is a thick film (~5000 Å) deposited on fused silica substrate. It is interesting to point out that μc-Si forms much more readily on stainless steel substrate [Curve (b)] than on an a-Si:H layer [Curve (c)].

In order to promote the formation of microcrystallinity on an a-Si:H surface where μc-Si doped layers are to be deposited in most device applications, we have developed an effective surface preparation method which allows immediate formation of μc-Si within the first 100 Å on a-Si:H. Curve (d) in **Figure 2.8** shows the Raman spectrum of a 100 Å μc-Si n-layer deposited on a 100 Å a-Si:H layer after the appropriate surface treatment. A large volume fraction of microcrystalline material was obviously formed in the ultra-thin layer which would have otherwise been amorphous without the surface treatment as shown by Curve (c) in **Figure 2.8**.

In order to obtain better utilization of the solar spectrum and to improve stability, two or more *p-i-n* junctions consisting i-layer materials of different bandgaps can be built in series to form a monolithic multijunction solar cell. The interface between the two junctions, often called the "tunnel" or recombination junction, is critical to the performance of the device. The doped layers in this recombination junction must support large electric fields extending into the intrinsic layers, in addition to the high field in the recombination junction itself.

10
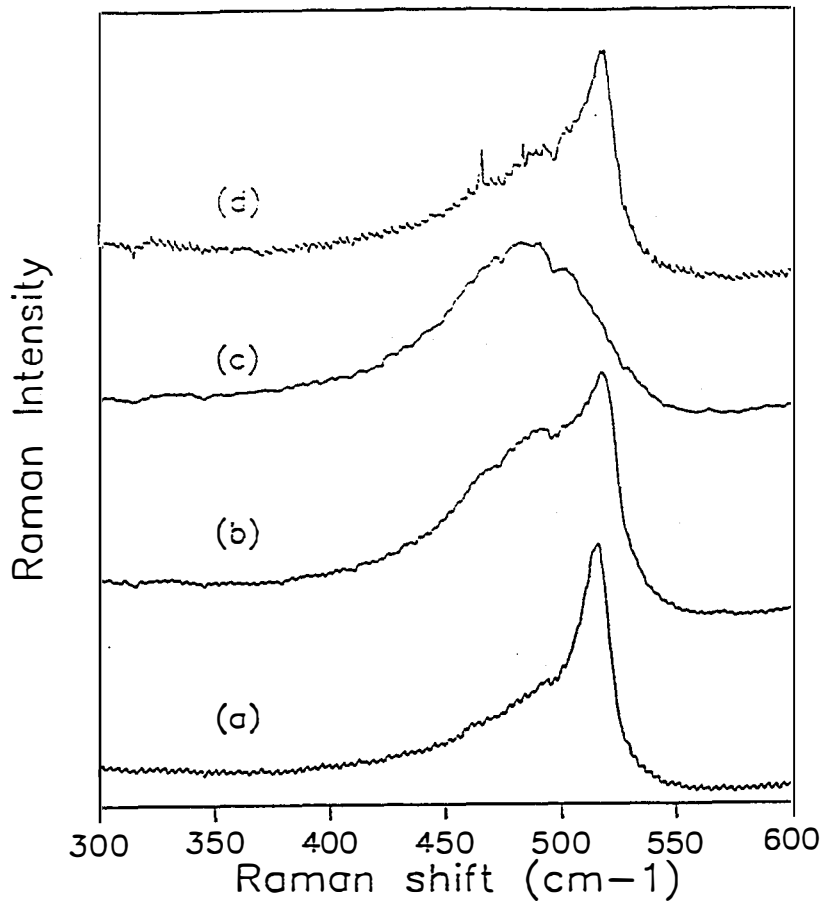
Figure 2.8 Raman spectra of films made under an n-type "microcrystalline" condition on various substrates: (a) a thick film on fused silica; (b) an ultrathin layer (~100 Å) on stainless steel; (c) same layer as in (b) made on a thin a-Si:H layer; and (d) same layer as in (b) made on a surface treated a-Si:H layer.

The interface region must promote efficient recombination of electrons, generated in the first i-layer, with holes from the second i-layer. Finally, the "tunnel" junction layers must have as little optical absorption as possible.

In the traditional amorphous multijunction device, improved results can be obtained by inserting a very thin, heavily doped p+ a-Si:H layer between the usual n_1 (a-Si:H) and p_2 (a-SiC:H) layers. The excessive boron doping in this thin layer reduces the effective bandgap slightly and also creates a very high density of defect states in the gap. Device analysis using a first-principles computer model indicate that the reduced bandgap of this layer would improve the supply of carriers required for efficient recombination, and thus improve performance [11]. The device model also indicates that the heavily doped layer promotes recombination directly via the high density of defect states in the energy gap and indirectly through recombination processes assisted by tunneling in these defect states.

11

The use of microcrystalline silicon in the doped layers of the recombination junction would be expected to offer several advantages: (1) The higher carrier density generally available in microcrystalline vs. amorphous Si would more easily support the high electric fields required while using very thin layers; (2) Efficient recombination would be promoted directly due to the smaller mobility gap and the increased doping density, and indirectly due to increased tunneling in the very thin layer(s); (3) The optical absorption loss due to the tunnel junction layers would also be reduced by using thinner layers, and due to the lower absorption coefficient of μc-Si in the visible wavelengths.

At open-circuit conditions the voltage of the multijunction solar cell should ideally be the sum of voltages developed across each *p-i-n* junction if there is no voltage drop across the tunnel junctions. However, for non-ideal tunnel junctions a significant voltage in opposite polarity with that generated by the *p-i-n* junctions in the device can occur due to accumulation of photocarriers near the tunnel junction, and thus reduce the open-circuit voltage [11]. Therefore, the high doping density and high electric field associated with the use of μc-Si in (1) above should improve V_{oc}. The effects listed in (2) above should improve the fill factor in a multijunction device because more efficient recombination in the "tunnel" junction will minimize charge accumulation near that junction. Thus, the external voltage required to support a given current is reduced in the device, i.e. a better fill factor. The third effect listed above would be expected to increase the short-circuit current of the tandem device.

We have recently fabricated multijunction devices using various combinations of μc-Si in the recombination junction, including the a-Si:H(n)/μc-Si(p), μc-Si(n)/a-SiC:H(p) and μc-Si(n)/μc-Si(p). Compared to a traditional tunnel junction using all amorphous materials, the junction using μc-Si n/a-SiC:H p yielded significant improvement in all aspects of device performance. **Figures 2.9** and **2.10** show the J-V characteristics and quantum efficiencies of two a-Si:H/a-Si:H tandem cells which are identical excepting the tunnel junction. The i-layer thicknesses for the two junctions are ~700 Å and ~3000 Å, respectively. As shown in **Figure 2.9**, the microcrystalline tunnel junction improved V_{oc} by almost 50 meV and raised FF from 69% to 72%. The short circuit current of the second junction, obtained by integrating the QE with an AM1.5 spectrum, is also increased by ~3% as shown in **Figure 2.10**. This increase in short-circuit current occurs at wavelengths expected to be influenced by tunnel junction absorption. All things combined, the incorporation of μc-Si improved the conversion efficiency of the tandem a-Si:H solar cell by more than 10% as shown in **Figure 2.9**.
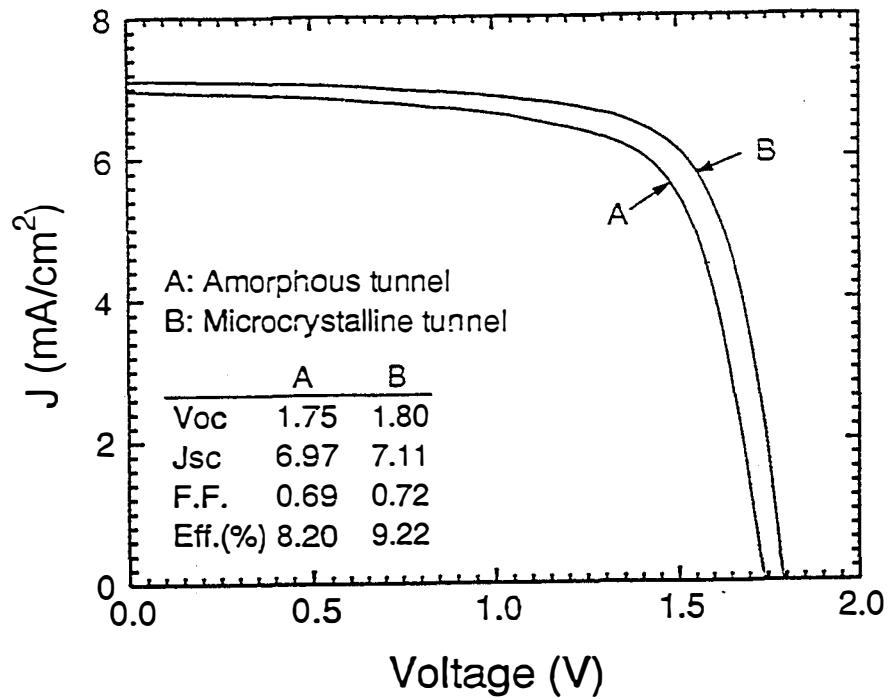
Figure 2.9 J-V characteristics of two Si/Si tandem solar cells. The only difference between the cells is that Cell A has an amorphous while Cell B has a microcrystalline tunnel junction. The cell parameters are listed in the Figure.
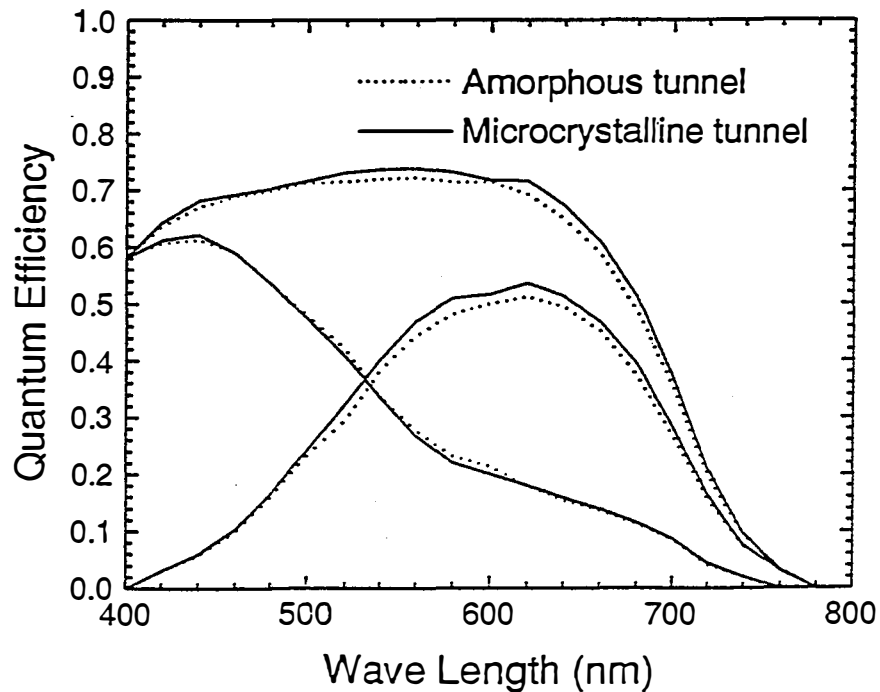
Figure 2.10 Quantum efficiencies as a function of wavelength for both junctions and the sum of the two for the same tandem cells as shown in **Figure 2.5.**

13

By incorporating the microcrystalline tunnel junctions into Si/Si/SiGe triple-junction cells and modules, we have achieved initial efficiencies of over 11% for those devices. **Figure 2.11** shows the J-V curve for one of such triple-junction cells.

2.4 "Fast" and "Slow" Defects in a-Si:H

Despite a great deal of progress made in recent years in understanding the metastable phenomenon in a-Si:H and its devices, new experimental results are constantly emerging, only to demonstrate that the "current" understanding is merely an approximation or a special case of a more complex phenomenon. For instance, the power law dependencies of the light-induced defect generation on exposure time and light intensity were first explained by a simple self-limiting bimolecular recombination mechanism [12]. However, it was later shown that this kinetic behavior can be alternatively explained by the stretched exponential (SE) kinetics which also successfully accounts for the defect saturation behavior after prolonged light soaking [13]. A key distinction of the stretched exponential kinetics is that it implies that defect generation and annealing processes in a-Si:H are dispersive, even though different microscopic mechanisms have been proposed to be responsible for the SE kinetics [13-17].

We present here new experimental data that cannot be described by any of the existing models including the stretched exponential kinetics. We demonstrate that a-Si:H is likely to contain more than one kind of defects which exhibit significantly different kinetics for creation and annihilation.
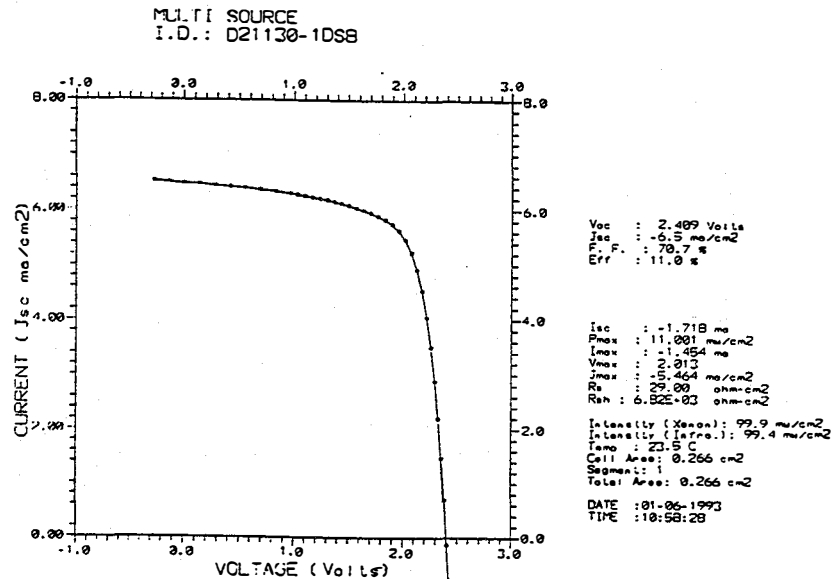
Figure 2.11 Initial J-V curve for a triple-junction cell incorporating microcrystalline tunnel junctions.

14

Thus, the total defect density is no longer a good parameter for describing the state of the material. Instead, simultaneous rate equations of all defect states and their initial conditions must be established in order to explain all experimental results consistently and make accurate predictions.

The key experiment revealing the interesting effect mentioned above consisted of two light soaking steps, i.e., an a-Si:H solar cell was first degraded under a high intensity light (typically at 50 suns) to a very low efficiency level and then exposed in the second step to the standard 1-sun intensity light. The temperature of the solar cell was maintained at ~50°C. The a-Si:H solar cells used in this study are simple *p-i-n* devices in which the *i*-layers are ~5000 Å thick and were made by d.c. glow discharge of pure silane (SiH_4) at 260°C. Details about the light soaking experiment have been published elsewhere [18].

Figure 2.12 shows the conversion efficiency (η) of such a solar cell subjected to pre-soaking, normalized by its initial value, as a function of exposure time under the 1-sun illumination (closed circles). The high intensity light soaking prior to the 1-sun illumination is not shown in this Figure. Also plotted in **Figure 2.12** is the degradation curve of an identical cell which was directly exposed to the 1-sun illumination from the as-deposited state (open circles). While the initial recovery of the cell degraded under high intensity light was expected, it was to our surprise that the recovery stopped after only ~100 hours of 1-sun illumination. With further illumination the cell efficiency even started to decrease, catching up with the other cell degrading from the as-deposited state. Finally, after ~1000 hours of continuous illumination both cells reached stabilization. The data shown in **Figure 2.12** cannot be explained by the existing theories for the kinetics of defect generation and annealing in a-Si:H. The majority of those theories [12-15] assume that the kinetic processes can be described by a single rate equation for the total defect density in the material. The stretched exponential kinetics, for example, results from a time-dependent rate equation such as the one shown below [13],

$$\frac{dN}{dt} = (\frac{t}{P})^{-\alpha}(G - DN) \qquad (1)$$

where α, P, G, D are all constants. However, such a rate equation cannot change the sign of the rate (dN/dt) during a fixed process. Once the rate reaches zero the system can no longer change and thus goes into the steady state. This is obviously in contradiction with the data shown in **Figure 2.12** where the sample subjected to the prior high intensity light soaking (closed circles) changed the sign of the derivative, dη/dt [=(dN/dt)(dη/dN)], when going through the maximum at ~100 hours. Here, the derivative dη/dN is assumed to be always negative.

15
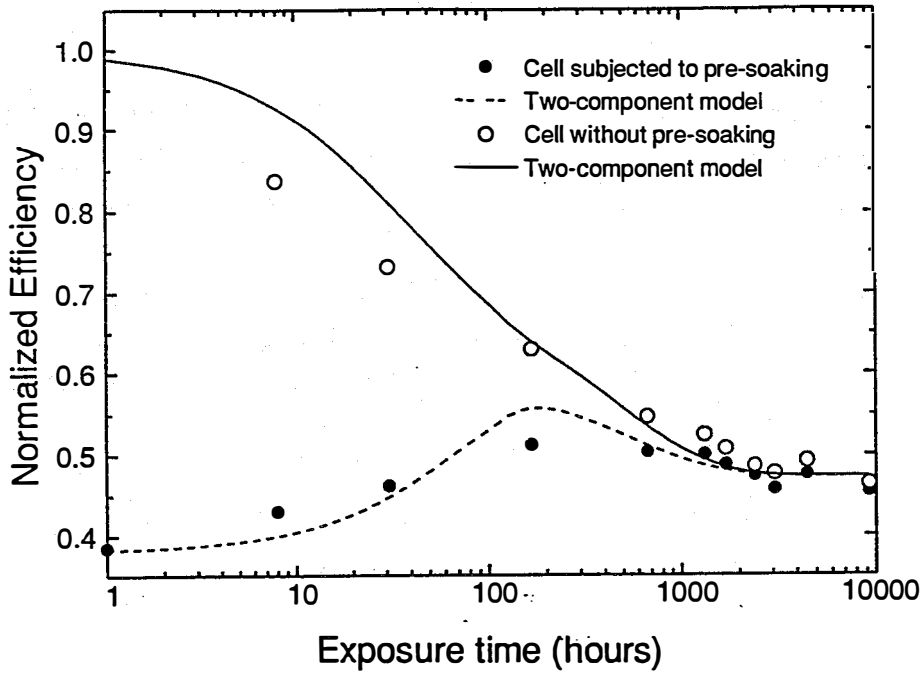
Figure 2.12 Normalized efficiencies of two identical solar cells as a function of exposure time under 1-sun illumination. One cell (closed circles) was light soaked for 2 hours at ~50 sun prior to the 1-sun illumination and the other (open circles) starts from the as-deposited state. The solid and dashed curves were calculated based on the two-component module discussed in the text.

The physical model underlying the above time dependent rate equation, **Eq. 1**, is that defect generation and annealing are controlled by a dispersive process such as hydrogen diffusion, but the material contains only one type of defects **[13-15]**. While the single-type defect models are inconsistent with our current observation, there is actually ample experimental evidence that the defect structure in a-Si:H is dispersive **[16,19-20]**. Namely, more than one type of defects with different kinetic characteristics in generation and annealing may be present in the material. Since each defect component follows an individual rate equation in this model, not only the total defect density but also its distribution among components would change during a kinetic process. Therefore, unlike in the single-type defect models the total defect density can no longer uniquely determine the state of material or be described by a single rate equation. Nevertheless, certain material and device properties, such as spin density, sub-bandgap absorption and solar cell efficiency, may depend solely on the total defect density but not on the detailed defect distribution. While there have been attempts to relate the stretched exponential kinetics with such a microscopic model, self-conflicting assumptions such as a fixed distribution of defects at all times **[16]** or a fixed set of initial conditions in all cases **[17]** can always been found in proving this relationship. As we will show in the following, this class of model can in fact explain well a

16

variety of complex kinetic phenomena including what is shown in **Figure 2.12** and be still consistent with all previous observations.

Although in reality the defect configuration in a-Si:H is likely to have a continuous distribution, we propose a simple two-component model as a first order approximation to illustrate the essential physics displayed in **Figure 2.12**. Namely, the total defect density due to light exposure is assumed to be the sum of two components, i.e., $N = N_1 + N_2$. Furthermore, we assume that all defects are generated from a common pool of ground states, and there is otherwise no direct communication between the two defect components. The system of rate equations for both components can thus be written as:

$$\frac{dN_i}{dt} = G_i(N_T - N_1 - N_2) - A_i N_i \qquad (\ i = 1, 2\ ) \qquad (2)$$

where G_i and A_i (i=1,2) are the constant defect generation and annealing coefficients for the *i*th component, respectively, and N_T is the total number of states which can be converted into defects. It should be noted, however, that the microscopic mechanism underlying the above system of rate equations, **Eq. 2**, is not limited to the one we have outlined here. Other models may have rate equations of the same mathematical form as in **Eq. 2**, although the meaning of the parameters can be somewhat different. These simultaneous rate equations can be solved analytically and the solution for N_1 and N_2 has the following general form,

$$N_i = N_i^s + C_i \operatorname{Exp}(-\frac{t}{\tau_1}) + D_i \operatorname{Exp}(-\frac{t}{\tau_2}) \qquad (\ i = 1, 2\ ) \qquad (3)$$

Where N_i^s is the stabilized defect density at t= for the *i*th component and the characteristic time constants, t_1 and t_2, are given by,

$$\tau_1^{-1} = A_1 + G_1 + \frac{(A_1 + G_1 - A_2 - G_2)}{2} \Delta \qquad (4)$$

where

$$\tau_2^{-1} = A_2 + G_2 - \frac{(A_1 + G_1 - A_2 - G_2)}{2} \Delta \qquad \begin{matrix}(5)\\(6)\end{matrix}$$

$$\Delta = \sqrt{1 + \frac{4\,G_1\,G_2}{(A_1 + G_1 - A_2 - G_2)^2}} \ - 1$$

17

The amplitudes, C_i and D_i ($i=1,2$), can be determined from the coefficients in the rate equations and the initial condition for a given process. The normalized cell efficiency can be related to the total defect density, N, using the semi-empirical relationship [22,23]

$$\frac{\eta}{\eta_0} = 1 - B \, Log(1 + \frac{N}{N_0}) \tag{7}$$

where B is a constant depending on the cell structure such as the i-layer thickness and N_0 is the initial defect density. For solar cells studied here B was estimated to be ~0.6 [22]. Assuming N_1 represents the so-called "fast" defects which can be generated as well as be annealed much faster than N_2, the "slow" defects, i.e., $G_1 \gg G_2$ and $A_1 \gg A_2$, then D becomes negligibly small and t_1 is much smaller than t_2. The total defect density which is the sum of the two would thus be largely controlled by the "fast" defects in the short time limit ($t < t_1$) and by the "slow" defects when $t > t_1$. The entire system reaches the steady state when $t > t_2$. In the experiment shown in **Figure 2.12**, for example, the high-intensity light soaking prior to the 1-sun illumination would produce more "fast" defects than "slow" defects. In fact, it would be possible that at the end of this period the density of "fast" defects is higher, whereas that of "slow" defects is lower, than the corresponding steady state density under the subsequent 1-sun illumination. If this happens, the total defect density would first decrease (cell efficiency increase) upon exposing to the 1-sun illumination because it is predominantly controlled by the "fast" defects when $t < t_1$. However, when $t > t_1$ the density of "fast" defects would stop decreasing and then the total defect density would turn to increase as the "slow" defects are gradually being generated. Finally, when $t > t_2$, the total defect density would level off as both defects approach the steady state. This is exactly what has been observed experimentally.

We have fitted the experimental data in **Figure 2.12** using the two-component model (the solid and dashed curves in **Figure 2.12**). While the fits obviously reproduced all the main features in the experimental data, the relatively large deviations seen in the beginning of both curves could be attributed to the over-simplification of the model which considers only two components rather than a continuous distribution. We note that the commonly observed power-law dependencies of defect generation on light intensity and time [12] can be easily reproduced when the appropriate intensity factor ($I^{1.8}$) is included in the G parameter and the results are plotted in terms of the total defect density. The parameters used in the fitting are listed in **Table 2.2**. The initial condition used was $N_1(0)/N_0 = 0$ and $N_2(0)/N_0 = 0$ for the as-deposited sample, and $N_1(0)/N_0 = 7.34$ and $N_2(0)/N_0 = 2.45$ for the sample which had been degraded by the high intensity light for two hours. Notice that the latter initial condition was set such that the ratio, $N_1(0)/N_2(0)$, was

equal to the ratio of the generation coefficients, G_1/G_2, because the period for the high intensity light soaking was much shorter than either of the characteristic time constants.

As we pointed out earlier, a direct consequence of the multi-component model is that the total defect density (or the solar cell efficiency) can no longer uniquely determine the state of material or device. In other words, depending on the history of treatment samples with the same total defect density may have different defect distributions and therefore produce rather different results when undergoing an identical process subsequently. Such phenomena, often referred to as "history dependencies", were difficult to understand in the past when total defect density was considered sufficient to determine the state of material. One such example is illustrated in **Figure 2.13** where we show the annealing results of two identical solar cells which were degraded to nearly the same efficiencies, however, using different light intensities and durations. Clearly, the cell which was degraded at ~50-sun intensity for 5 minutes (solid squares) annealed significantly faster than the other which was degraded at 1-sun intensity for 100 hours (open circles). This is again consistent with the two-component model because light soaking at high intensity for a short period would produce a larger portion of "fast" defects than at low intensity for a much longer period, resulting in the observed stronger initial recovery. In fact, the universal shape of the annealing curves, which consists of a fast initial rise and a long tail, [19] is itself a manifestation that at least two characteristic time constants are involved in the process. In terms of the two-component model, the "fast" defects are naturally responsible for the fast initial recovery and the "slow" defects for the long tail. The solid and dashed curves in **Figure 2.13** were calculated from the two-component model that is consistent with the one used to fit the data in **Figure 2.12**. The parameters of the rate equations are again listed in **Table 2.2**. The initial conditions, $N_1(0)/N_2(0) = 3$ under the high intensity and $N_1(0)/N_2(0) = 1.5$ under the low intensity, were directly derived from the previous case. The annealing coefficients at 130°C are, on the other hand, larger than their counterparts at 50°C by a temperature activated factor with the barrier energy ~1 eV. However, the fact that the ratio A_1/A_2 remained roughly the same at both temperatures indicates that the difference between the two defect states may not be in the barrier energy but rather in the pre-exponential factor. The two-component model also agrees well with a number of other common observations in annealing experiments such as that the cells degraded at higher temperatures or for longer durations are more difficult to anneal than those degraded at lower temperatures or for shorter durations [20].

It is interesting to note that recent studies have indicated that the kinetics of light induced degradation in a-Si:H depends on the preparation conditions [24,25]. For example, samples made with hydrogen dilution can be stabilized much sooner, i.e. after ~100 hours of 1-sun illumination, than those discussed in this section which were made without H_2-dilution. This observation can again

19

be easily explained in terms of the two-component model [25]. The fact that stabilization occurs at ~100 hours which is roughly the characteristic time for the "fast" defects suggests that there are few "slow" defect states in samples made with H_2-dilution. With this interpretation, any structural difference between the two materials may be identified as the potential source for the "slow" defects.
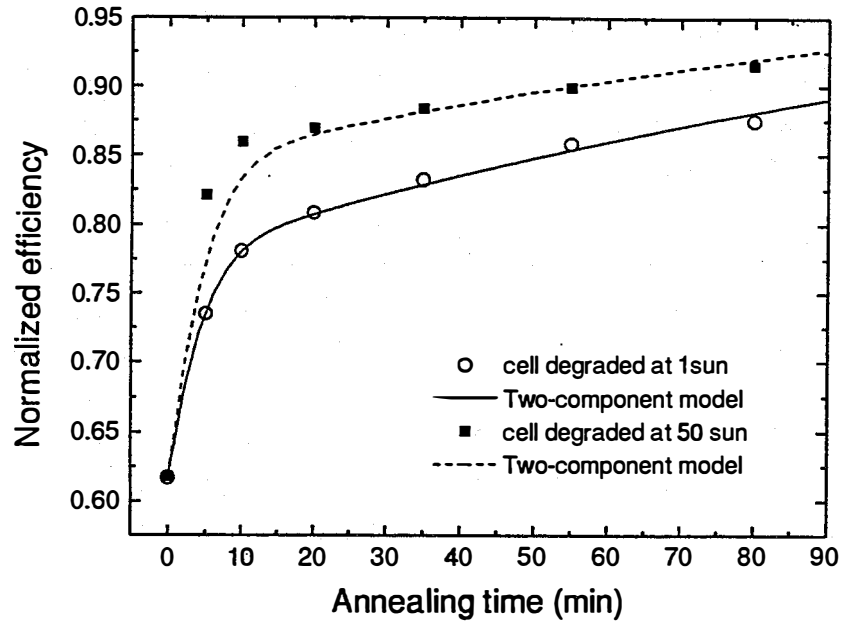
Figure 2.13 Normalized efficiencies as a function of annealing time at 130°C for two solar cells which were degraded to the same efficiency using different light intensities and duration. One cell (closed circles) was light soaked at 50 suns for 5 minutes and the other (open circles) at 1 sun for 100 hours.

Table 2.2 Parameters of the two component model used to fit data in **Figures 11 and 12.**

	1 Sun, 50°C	Dark, 130°C
G_1 (hr^{-1})	3.0×10^{-3}	0
A_1 (hr^{-1})	1.4×10^{-2}	1.7×10^{1}
G_2 (hr^{-1})	1.0×10^{-3}	0
A_2 (hr^{-1})	7.2×10^{-4}	6.3×10^{-1}
τ_1 (hr)	57	5.8×10^{-2}
τ_2 (hr)	654	1.6
N_T/N_O	10.6	10.6

20

3.0 Task II: NON-SEMICONDUCTOR MATERIALS RESEARCH

3.1 Introduction

Non-semiconductor materials research includes development of front and rear contacts for multijunction solar cells and modules. A number of significant improvements have been made in the front and in the rear contacts used for a-Si based multijunction solar cells and modules over the past year. The most important results include: (1) The development of an improved recipe for our standard tin oxide front contact that allowed us to demonstrate 4% higher cell efficiencies. (2) The discovery that the uniformity of ZnO films for front contacts deposited using atmospheric-pressure chemical vapor deposition (APCVD) is greatly improved by using appropriate selection of the oxygen-supplying feedstock. (3) The deposition of uniform, powder-free ZnO films for front contact on 1000-cm^2 substrates using low-pressure chemical vapor deposition (LPCVD). (4) Quantification of the optical losses from the front and the rear contacts which led to the conclusion that the red response can be improved by increasing the reflectivity and scattering of the ZnO/Ag rear contact.

The greatest opportunities for additional improvement in contacts are in the following areas: (1) The development of a thinner ZnO film having sufficient haze for use as a front contact in order to take greater advantage of zinc oxide's high transparency. (2) The improvement of the ZnO/p interface in order to avoid fill factor losses. (3) The improvement of the ZnO/Ag rear contact that will allow us to use a higher bandgap alloy for the rear cell of a multi-junction device.

3.2 Approaches to Improving Non-Semiconductor Materials

In order to improve the front contact and the rear contact, we have worked in the following four areas:

1. Optimization of present APCVD SnO$_2$ front contact.
2. Development of APCVD process for ZnO front contact.
3. Development of LPCVD process for ZnO front contact.
4. Improvement of the ZnO/Ag rear contact.

Since earlier work had provided a proof-of-concept for the potential of ZnO to improve device efficiency [26], we devoted much effort to the development of an APCVD process for ZnO front contact deposition. We hoped that this effort would allow us to convert our Watkins-Johnson

21

belt furnace from tin oxide to zinc oxide, providing us the advantage of a better front contact without a major expenditure for capital equipment. When it became apparent that problems related to uniformity, haze formation, and powder production were not easily tractable, we decided to try to improve our understanding of the APCVD process which we use to deposit SnO_2. This approach had two advantages: (a) We expected to gain insight into those issues affecting film uniformity and haze formation which would be transferrable to an APCVD ZnO deposition process, and (b) we expected that optimization of the SnO_2 made in our R&D furnace would be easily transferrable to our manufacturing line.

By optimizing the tin oxide front contact we were able to improve solar cell efficiency by about 4%. The recognition of the roles of the individual feedstocks in the SnO_2 deposition process provides a lead for the approach which we should take if we ever return to the development of an APCVD process for the deposition of ZnO. We eventually decided to try to develop a low-pressure chemical vapor deposition process (LPCVD) for ZnO. This process avoids the problem of powder formation and greatly reduces the impact of the gas-phase reactions which complicate the APCVD of ZnO. We decided to construct a belljar system which can handle 12" x 13" substrates so that any process developments could be easily transferred to large-area modules. This system was running by early June 1993, and system modifications were made by the end of June 1993 which allowed us to deposit uniform films over a 12" X 13" area.

3.3 Optimization of APCVD process for SnO_2 front contact

Our standard tin oxide front contact consists of two layers: a specular layer 2000 Å to 3000 Å thick, followed by a textured layer 6000 Å to 8000 Å thick. In the past year, we have demonstrated that optimization of the tin oxide front contact can improve device efficiency by about 4%, primarily by improving the transparency of the front contact. Two changes to the tin oxide recipe were responsible for this improvement:

1. Improvements in the uniformity and transparency of the specular layer.
2. An optimization of the dopant distribution in both the specular and textured layers.

Our study of the APCVD process for tin oxide provided us with important insights which may be useful for zinc oxide deposition by this process. Two features of this process were recognized: (1) The importance of a uniform underlayer to aid nucleation, and (2) the significant role of a moderator to limit the gas-phase reactions (and thus limit powder formation) during the deposition of the specular layer.

By optimizing the deposition of the specular layer, we were able to achieve good uniformity at a thickness of only 1000-1500 Å, consequently improving optical transmission. Optical transmission at wavelengths greater than about 700 nm is adversely affected by the presence of excess dopant in the oxide. Thus, the amount of dopant should be limited to that necessary to produce a desired low sheet resistance. We found that light doping of the textured layer contributes significantly to the overall conductivity of the film, contrary to past experience, thus allowing us us to reduce the doping of the underlayer. It was also found that heavy doping changes the morphology of the film, leading to a less hazy film than would be observed in a more lightly doped film of comparable thickness.

An experiment to compare "optimized" tin oxide with our standard tin oxide was carried out. An a-Si:H single-junction cell was co-deposited on both kinds of tin oxide in three different runs in one a-Si deposition system. The top three cells made on each kind of tin oxide were compared. The results are summarized in **Table 3.1**. Each entry in the table is an average of three cells on each of three different 3"x3" substrates.

Table 3.1 A comparison of our best cells made on standard tin oxide and our best cells made on optimized tin oxide.

a-Si Run #	Average of top three cells on optimized CTO				Average of top standard CTO				Difference in Efficiency
	V_{oc}	FF	J_{sc}	Eff.	V_{oc}	FF	J_{sc}	Eff.	%
C3154-2	0.863	0.721	15.35	9.56	0.869	0.707	14.94	9.17	4.3
C3155-1	0.870	0.733	15.26	9.74	0.862	0.736	14.94	9.48	2.7
C3155-2	0.874	0.734	15.13	9.70	0.872	0.704	14.86	9.13	6.2

3.4 Development of APCVD process for front contact of ZnO

For amorphous silicon based thin-film photovoltaic applications, the transparent, conducting metal oxide front contact has usually been prepared with a textured tin oxide film. Zinc oxide is an

alternative material that offers both optical and electrical advantages over tin oxide. Because zinc oxide has a larger band gap, (2.2 eV versus 2.0 eV for tin oxide), ZnO is more transparent at lower wavelengths. Throughout the entire spectrum ZnO films absorb less light than tin oxide films with the same film thickness as shown in **Figure 3.1**. In addition to its physical properties, zinc oxide has numerous chemical advantages over tin oxide. Because zinc oxide is known to be chemically more resistant to reduction than tin oxide, zinc oxide is expected to be more stable in the silane plasma that occurs during a-Si deposition. From a materials handling and manufacturing point of view, the use of zinc oxide makes possible a less corrosive environment because hydrochloric acid is not created as a deposition by-product. Zinc oxide's solubility in dilute acid solutions simplifies equipment clean up and maintenance.
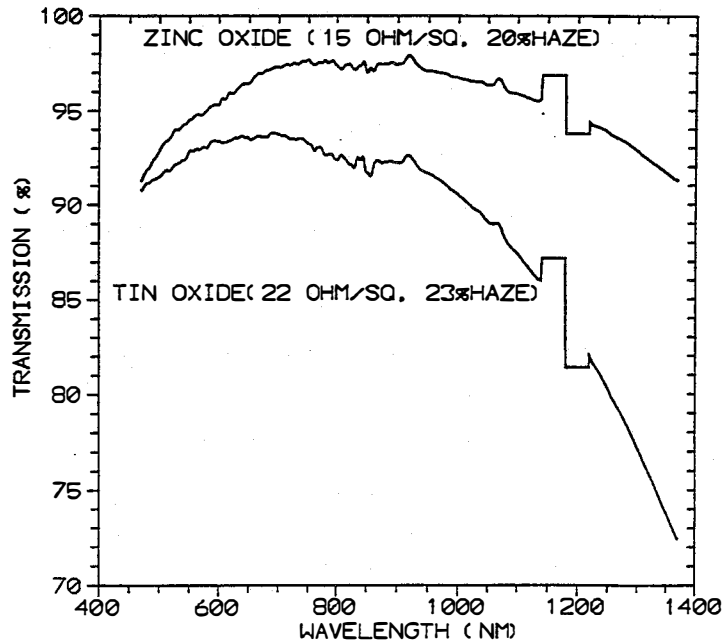
Figure 3.1 Transmission of Tin Oxide and Zinc Oxide

On the other hand, zinc oxide will probably be slightly more expensive than tin oxide because the feedstock diethylzinc (DEZ) costs more than tin compounds. The pyrophoric material DEZ requires special handling. Zinc oxide is known to be slightly hygroscopic and to react with water. It remains to be demonstrated that a zinc oxide front contact can be sufficiently well sealed to prevent degradation during the lifetime of a photovoltaic module.

24

The parameter space which is associated with APCVD of zinc oxide is extremely large and so far we have explored only portions of it. These include feedstocks and their flow rates, and system parameters such as exhaust rate and deposition temperature. A general problem initially was lack of day-to-day reproducibility, indicating a lack of process control, and making optimization impossible. However, alternative feedstocks were found which reduced this problem substantially. Our results suggest that APCVD zinc oxide depositions are encountering problems with a reaction that is controlled by gas diffusion rates and not by the chemical kinetics of deposition.

3.5 Development of LPCVD process for ZnO front contact

Low-pressure chemical vapor deposition (LPCVD) of zinc oxide was examined as a way to remove the effects of gas diffusion and make the reaction kinetically controlled. In order to completely avoid the problems of powder formation and the difficulty of making uniform depositions which were encountered using the APCVD process to deposit SnO_2 and ZnO, we decided to build an LPCVD system. The apparatus uses a belljar with standard vacuum technology. Nitrogen is used as the carrier gas for all reagents. The literature reports a wide range of LPCVD zinc oxide depositions techniques carried out at 1 to 150 torr. At lower pressures, diffusion of gases is more rapid than at one atmosphere and is not expected to limit the rate of deposition.

This belljar system is capable of handling 12x13 inch substrates, so that any process developments can be easily transferred to large-area modules. This system was running by early June 1993 and system modifications were made by the end of June 1993 which allowed us to deposit uniform films over a 12x13 inch area.

The LPCVD deposition of zinc oxide produced excellent films. The results were very uniform and reproducible in the substrate temperature range of 150-170°C. The haze obtained was directly related to the thickness so square-foot uniform films of varying haze could be deposited. It has been possible to prepare films on a wide range of zinc oxide films. The results are presented in **Table 3.2**

25

Table 3.2 Comparison of a cell prepared on APCVD Tin Oxide and 2 cells on LPCVD Zinc Oxide.

	APCVD Tin Oxide	LPCVD Zinc Oxide	LPCVD Zinc Oxide
Transmission (%)	79	83	81.5
Haze (%)	16	15	31
Resistance (Ohm/Sq)	22	15	13
Fill Factor	0.74	0.74	0.69
V_{oc} (V)	0.94	0.91	0.91
J_{sc} (mA/cm^2)	10.5	11.1	11.4
Efficiency (%)	7.3	7.4	7.2

It is clear that the zinc oxide films are more transparent and produce cells with significantly higher currents (J_{sc}). Work is continuing to improve the fill factors and the open-circuit voltages (FF and V_{oc}) on the cells.

3.6 Comparison of front contacts prepared by two different processes.

During this period, we have studied front contacts prepared by APCVD (SnO_2 and ZnO) and LPCVD (ZnO).

Table 3.3 shows a comparison of film properties of SnO_2 prepared by APCVD, ZnO prepared by APCVD and ZnO prepared by LPCVD. Some general observations can be made. First, ZnO films are more transparent than SnO_2, as expected. Second, LPCVD films are very uniform. Third, APCVD ZnO is not the same as LPCVD ZnO. The LPCVD film has to be thicker (so far in our investigations) than APCVD films to achieve the same texture, hence it has less transmission.

Table 3.3 Selected Properties of APCVD Tin Oxide and Zinc Oxide Films and LPCVD Zinc Oxide Films.

	APCVD TIN OXIDE		APCVD ZINC OXIDE		LPCVD ZINC OXIDE	
Resistance	13	16	14	18	16.5	14.5
Haze (%)	23	16	15	11	24.5	19
Transmission (%)	79	82	82	86.5	82	83
Thickness (μm)	0.84	0.56	0.86	0.51	1.5	1.5
Optical Uniformity	Good	Good	Poor	Poor	Very Good	Very Good
Sample #	93146B	93146Q	92206E	92188F	93237E	93231C

It appears that substrate composition and crystallite initiation are important factors in haze growth. If APCVD ZnO is grown on glass substrates it is possible to get some nonuniform haze growth. If a specular layer of ZnO (deposited either by sputtering or APCVD) is first deposited and then the film is run through the furnace with other glass substrates, the glass substrates will have the expected haze, but the films with the underlayer of specular ZnO will show no haze, regardless of how thick the ZnO is grown.

Another factor controlling haze growth is the crystallographic orientation of the ZnO film. Based on x-ray powder studies carried out at the Institute of Energy Conversion, University of Delaware, APCVD deposited ZnO grow along the 002 axis forming hexagonal columns. In contrast, **Table 3.4** shows that zinc oxide grown by low pressure chemical vapor deposition (LPCVD) grows along the 110 axis. As described in earlier sections, LPCVD ZnO was found to produce excellent haze under some conditions.

Table 3.4 ZnO Orientation

Sample No.	Source	Dopant	Thickness (μm)	Peak #1 Index/ Relative Intensity	Peak #2 Index/ Relative Intensity	Peak #3 Index/ Relative Intensity
1978	LPCVD	B	1.1	(110)/0.85	(100)/0.15	
1806	LPCVD	B	1.7	(110)/0.92	(100)/0.08	
92-155A	APCVD	F	0.55	(002)/1.00		
92-170J	APCVD	F	1.1	(002)/0.63	(101)/0.20	(100)/0.17
92-164E	APCVD	F	1.1	(002)/0.76	(101)/0.24	

Efforts were made to prepare zinc oxide films with low resistances and high transmissions. **Figure 3.1** shows the visible spectra of typical zinc oxide and tin oxide samples in index matching fluid (diiodomethane) which is used to eliminate the effect of light reflection and light scattering (typically 7-15% of the incident light). The transmission of light by a zinc oxide film is significantly better than that of a tin oxide film with comparable haze and resistance. Except for the blue portion of the spectrum (under 550 nm), the zinc oxide film absorbs less than 5% of the incident visible light.

A rapid single value for transmission over the visible spectrum was obtained from the hazemeter, (Hazegard Hazemeter, Gardner Co., Silver Spring, MD) at the same time that a haze measurement was made. The following expression defines transmission and absorption:

Absorption = 1 - Transmission - Reflection - Scattering

28

The values of transmission in **Table 3.2** and **Tables 3.3** were obtained in air and do not take into account losses by light reflection or scattering. These losses are essentially the same for similar samples so transmission values in air are useful for comparing samples.

When there is a question of optical losses and absorption, the samples were immersed in a cell with the index matching fluid diiodomethane before taking the transmission on the hazemeter. In the above equation the reflection and scattering terms approach zero so that absorption does equal 1-T. **Table 3.5** describes several APCVD zinc oxide low resistance films whose transmissions were obtained using index matching fluid. These highly doped films were unsuitable for preparing cells because they have low haze and poor optical uniformity. As indicated in **Table 3.5** the best film had a resistance of 6 ohm/sq and an absorption of 4.9%. LPCVD zinc oxide films have to be very thick to achieve low resistances and transmissions were generally low.

Table 3.5 Selected APCVD Zinc Oxide Films with Low Resistances.

Resistance (ohm/sq)	4	6	9
Film Thickness (μm)	1.37	0.73	1.05
Haze (%)	2	8	7
Transmission (%) (run in index matching fluid)	91.1	95.1	94.6
Absorption (%)	8.9	4.9	5.4
Optical Uniformity	poor	poor	poor
Sample #	92266d	922203k	92283b

3.7 Improvement of the ZnO/Ag rear contact

Our efforts to improve light trapping and increase J_{sc} involved (i) QE and I-V measurements on cells with different rear contacts, (ii) spectroscopic measurements of specular and diffuse reflectance and transmission on cells with and without rear contacts, and (iii) fitting

29

experimental QE and optical data to calculations using a model incorporating geometric optics. The objectives were (i) to determine the relative importance of interface vs. rear contact scattering in multijunction cells and (ii) to quantify and reduce optical losses in the rear contact.

We have previously evaluated different rear contacts and obtained optimum red response in QE's using ITO/Ag [27]. Subsequently, we have obtained similar results using ZnO/Ag as the rear contact. We extended this study by investigating the effects of ZnO and Ag deposition conditions and ZnO thickness on J_{sc}. We find that ZnO/Ag rear contacts yield ~5% higher current compared to Ag. As the ZnO thickness (d_{ZnO}) is varied from 200 to 2000 Å, the red response (QE at 700 nm) varies by ~10%, with the optimum performance being obtained for d_{ZnO} ~ 1000 Å. For cells with a very thin ZnO there is a substantial drop in the fill factor. We believe this is due to the poor conductivity of very thin ZnO layers. Over the range of deposition conditions we examined, the cell parameters were not very sensitive to the other details of rear contact deposition.

We have previously developed a model to determine optical absorption in various layers in a multi-junction solar cell [28]. This model is based on geometric optics and uses independently measured optical constants and thicknesses of the layers as the input. The spectral dependence of interface and rear contact scattering are incorporated in the model, based on measurements on appropriate samples in liquids with different refractive indices. We have modified this model to calculate as a function of wavelength, optical absorption in the i-layers (assumed to be the cell QE) and specular and diffuse reflectance and transmission of the complete cell structures. We get good agreement between experimental and calculated spectra for all these parameters. As an example, **Figure 3.2** shows a comparison between calculated and measured reflectance spectra for a single-junction a-Si cell with a ZnO/Ag rear contact. The experimental data show weak interference fringes in total and specular reflectance spectra due to partial coherence of light in the rough sample. When averaged through these fringes, the experimental data agree rather well with the calculations. Similar measurements on cells deposited on SnO_2 with varying degrees of roughness show that most of the light scattering at long wavelengths occurs upon reflection at the rear contact. We thus expect further improvements in red response with continued optimization of the rear contact.
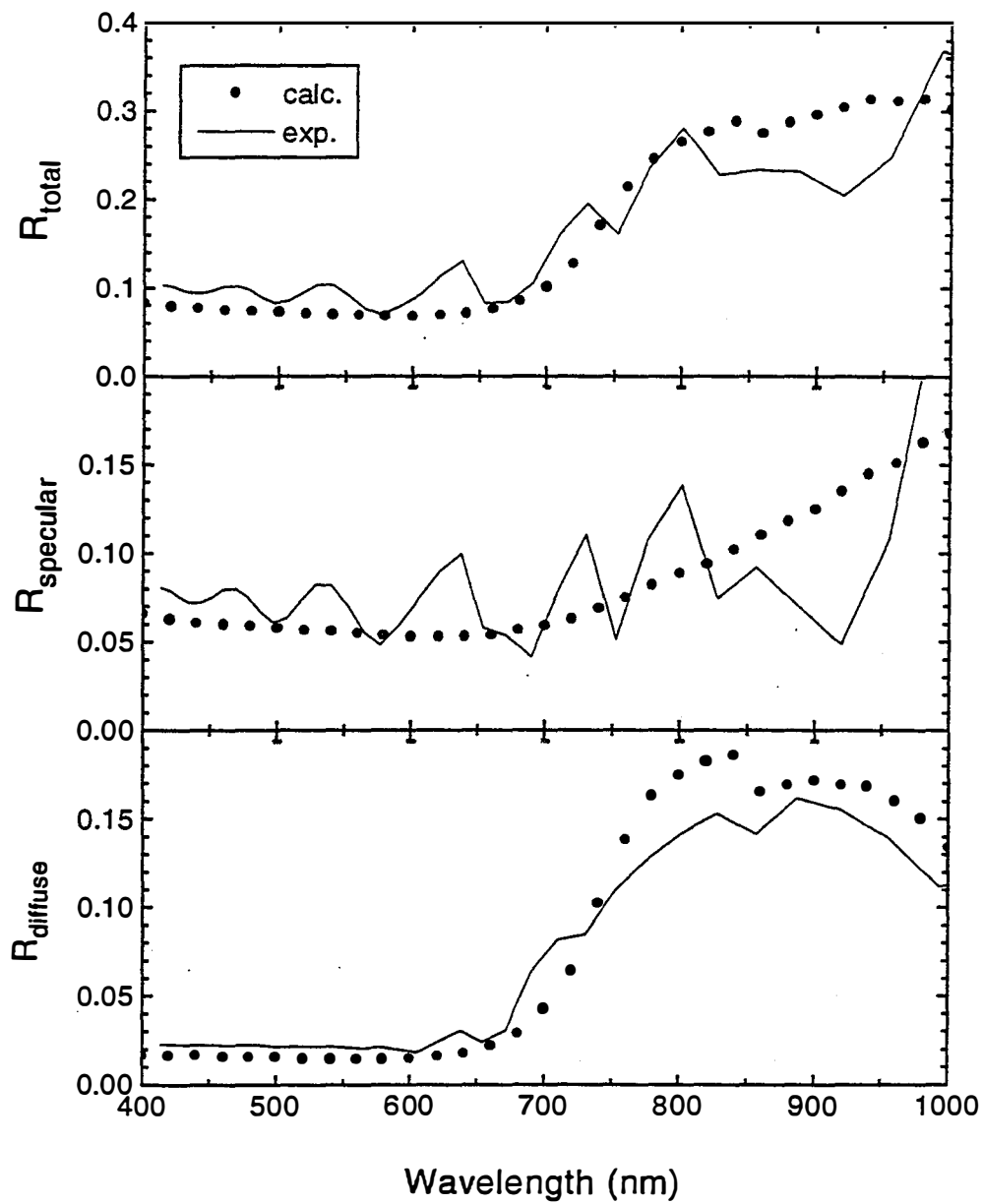
Figure 3.2 Total, specular, and diffuse reflectance spectra for an a-Si cell with ZnO/Ag rear contact.

4.0   Task III: MODULE RESEARCH

4.1   Introduction

Triple-junction small-area cells (0.26 cm^2) and modules (860 cm^2) have been made with initial conversion efficiencies in excess of 11%. These cells and modules have the following device structure: Light ===> glass/CTO/a-Si/a-Si/a-SiGe/ZnO/Ag.

We have used both soda-lime glass and low iron glass as substrates, generally in the thickness range of 60-83 mils. The modules are divided into 24-26 segments and interconnected by a 3-step laser scribing technique. **Table 4.1** shows the characteristics of some of the best modules and a comparable small-area cell.

Table 4.1   Initial characteristics of some of our best triple-junction a-Si/a-Si/a-SiGe modules and a comparable small-area cell.

Module #	V_{oc} (V)	FF	I_{sc} (mA)	Aperture Area Eff (%)	Aperture Area (cm^2)
D3091-2	63.23	0.676	209.5	11.35	789.1
D3078-2	58.56	0.682	206.7	11.34	728.4
M3067-1	62.97	0.669	226.3	11.05	862.7
M3061-1	62.75	0.685	203.0	11.05	789.1
Cell #	**Voc** (V)	**FF**	J_{sc} (mA/cm^2)	**Eff** (%)	**Area** (cm^2)
D11130-1	2.42	0.69	6.7	11.15	0.26

In these modules we have incorporated deposition of a-Si:H i-layers at low temperature from SiH$_4$ diluted in H$_2$. Microcrystalline n-layers were incorporated in the tunnel junctions. The I-V characteristic of one of the best of these modules is shown in **Figure 4.1**. The best modules are comparable in efficiency to the best small-area devices.

ID. No. D3091.2
Voc = 63.23 V
Isc = 289.5 mA
FF   = .676
Ef,ap= 11.35 %

Sun = 100 mW/cm2
Temp = 24 degC, 24
Segs = 26
Aper. Area/Seg
     = 38.35 cm2

83-31-93

CURRENT (Amps)

VOLTAGE (Volts)
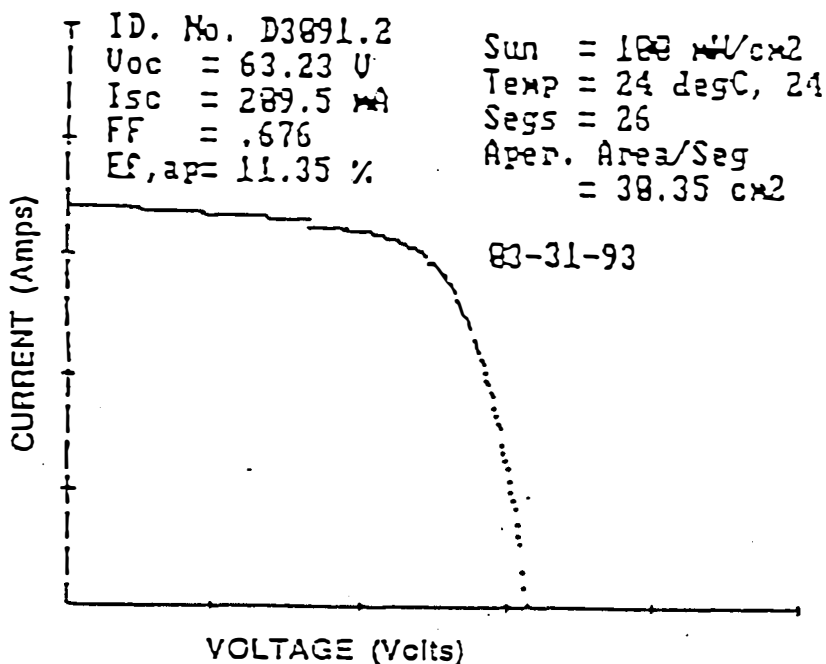
Figure 4.1 J-V characteristics of an 11.3% triple-junction module D3091-2.

Interconnects consume only 2.3% of the active area of the module. Using this interconnect scheme we have achieved fill factors greater than .70. An example is module #M3245-1 a Si/Si/SiGe structure with FF = .705 and efficiency 10.58%

4.2 Measurements

There has been some question about efficiency measurements and round robins were in progress in June 1993 to compare the simulators at various facilities. In light of discrepancies between various indoor simulators we tried to confirm our conversion efficiency measurements by measuring our modules outdoors on a clear day and scaling the currents by appropriately measuring the solar spectrum on that day. We obtained satisfactory agreement as shown in **Table 4.2**.

33

Table 4.2 A comparison of indoor and outdoor measurements on a particular 12 x 13 inch triple-junction module, D3091-2.

	V_{oc} (V)	FF	I_{sc} (mA)	Efficiency (aperture area) (%)
Spire	63.23	0.676	209.5	11.35
Outdoors	62.2	0.697	201.2	11.05

Insolation was measured by means of filtered (BG38) crystalline solar cell calibrated by NREL. The current shown in **Table 4.2** for outdoor measurements was scaled to 1000 W/m^2. The lower V_{oc} measured outdoors is most likely simply the result of module heating in the sun. Once a module is exposed to sunlight its temperature rises very rapidly and V_{oc} decreases. The higher fill factor may be related to spectral differences. Overall agreement between our Spire simulator and outdoor measurements is satisfactory.

4.3   Stability

High-efficiency small-area triple-junction cells lose about 15 - 18% of their initial efficiency. **Figure 4.2** shows the efficiency as a function of time for a small-area triple-junction cell which retains in excess of 9% efficiency after 600 hours of light soaking.

Triple-junction modules which lose 15 - 18% of their initial efficiency have been made (see, for example, **Figure 4.3**). The highest efficiency triple-junction modules however typically lose 20 - 25% of there initial efficiency (**Figure 4.3**). This increased degradation could arise from a number of sources. There is nothing in the structure of these cells which is particularly different than those which lose 15 -18%. The additional loss is due to some non-Staebler-Wronski component of degradation. We believe that shunts which are always present to some extent in modules, are the source of the additional losses in efficiency. Other possible sources, such as laser scribing, mishandling, etc. have been investigated but not implicated.
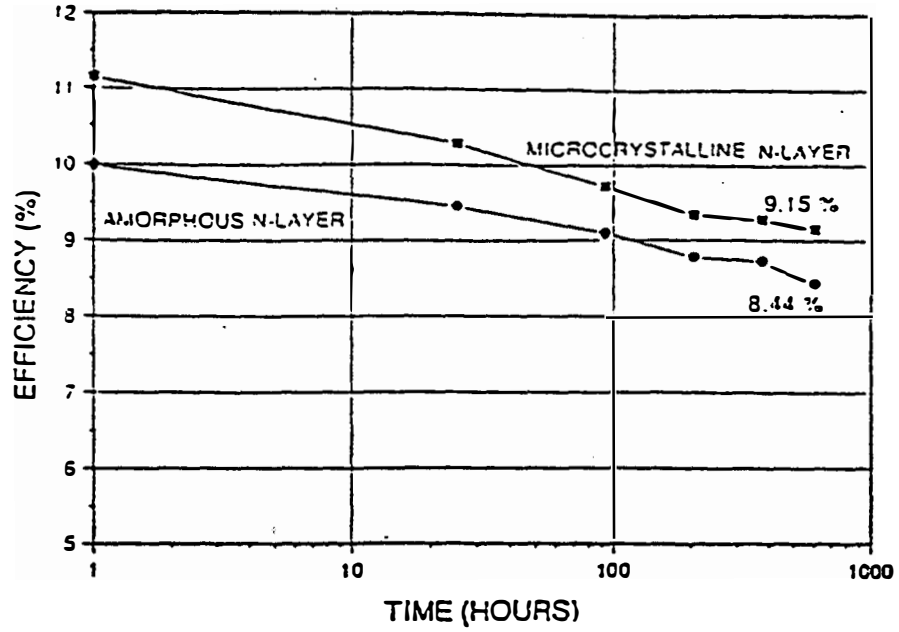
Figure 4.2 Efficiency versus time curve for high-efficiency triple-junction cells with and without microcrystalline n-layer at tunnel junction.
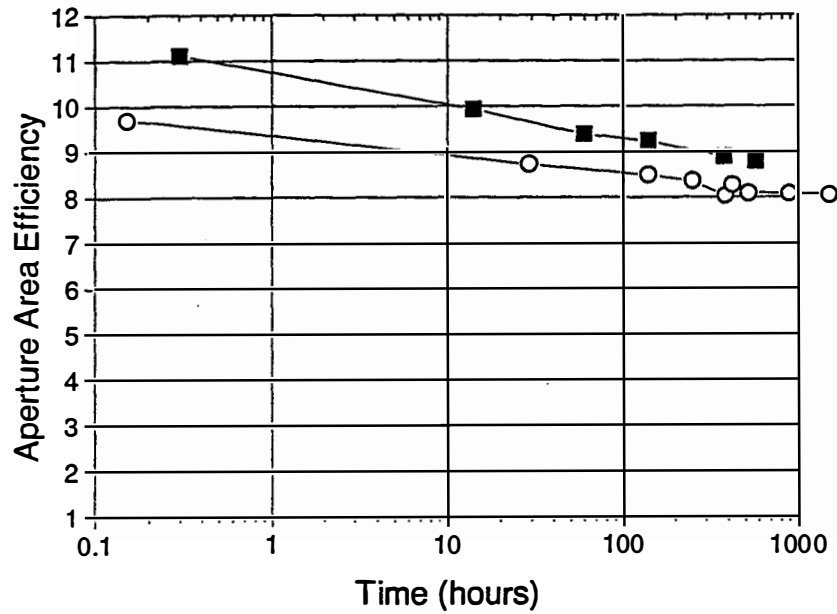

Figure 4.3 A triple-junction module with initial efficiency around 10% showing about 18% loss and stabilization after about 300 hours. Modules with initial efficiency in excess of 11% show slightly higher rates of degradation.

35

4.4 Scale-up

Notice that there is no loss in scaling from less than 1 cm^2 to nearly 1000 cm^2. This is a result of several factors.

1. The cells and modules are made in the same deposition system, hence there are no concerns connected with transfer of recipe.

2. The uniformity of tin oxide, a-Si, and rear contact is good.

3. Very little active area is lost to the laser pattern.

4. Laser patterning introduces no losses in fill factor or open-circuit voltage.

5. Small-area devices cut out of modules show higher currents than small-area cells made as such, when measured on the same apparatus and in the same way. The causes of this effect are unknown.

4.5 Uniformity

Some problems with uniformity were encountered when we switched to low temperature H_2-diluted SiH_4 deposition. These non-uniformities had a significant effect only on red response (about 30%) and were the result of changes in i-layer thickness and perhaps, to a much lesser extent, variation in bandgap. These effects initially were compensated for by making the i-layer of the back junction generate excess current using a (thicker layer or a lower bandgap layer. While compensating for non-uniformities, there is a slight loss of efficiency. However, more recently we have found that these effects are related to reactor geometry and that various small adjustments in the reactor configuration can substantially reduce these effects.

4.6 Shunts

Shunting is of practical importance both for its effect on initial efficiency (or yield) of modules or small-area devices and for its effect on photodegradation. Initial efficiency is adversely affected by large, generally discrete, defects. Stable efficiency, on the other hand, is affected by smaller defects which are often clustered together in fields and which do not affect the initial efficiency significantly.

The effect of shunts on module stability is estimated to be 3-5% in addition to the normal Staebler-Wronski loss. We arrived at this by first observing that the best small area diodes and modules degrade 16-18%, while typically modules lose 20-25%. Furthermore, we observe that degraded modules, if "cured" segment by segment showed a recovery of some or all of this additional loss. The longer a module is degraded, the greater the risk of shunt-induced degradation, and the greater the possible loss resulting from it.

By looking at the dark I-V characteristic of each segment of a module it is easy to locate the segments which contain shunting defects. We have reported previously [26] that when segments are shunted, the defects are almost always located in the 1-inch strip around the perimeter of the modules. It has been found, except in extreme cases where there were many pinholes or large amounts of debris, that there is no correlation between the segments which are shunted and the segments in which the pinholes and/or debris are found. When a 1-inch perimeter laser scribe has been made removing the outer edge of the module from the active area, and a shunt still exists, it is often identifiable as a point defect somewhere in the interior of the module. We have investigated the causes of the defects in the perimeter region. Again, we did it by scribing the outer rejected part of each segment into several smaller segments (**Figure 4.4**). We have not developed specific shunt repair methods beyond isolating them at the edge. We found that in many cases the segment problem arose at the very edge of the module where there is a thickness problem due to non-uniformities in the a-Si deposition around the edges of the module. However, the remaining shunts seem to be caused by discrete shunting defects (rather than fields of smaller defects). While these larger shunt-causing defects can exist anywhere on the module they seem to be preferably located close to the module edges. The cause of these origin of these defects is unknown. However it has been found that scratches, abrasions and impacts resulting from electrical contacting of these cells and segments with probes has little or no effect on shunting unless the mechanical damage crosses the edge of a segment.

The second effect of shunts is to provide an enhanced rate of photodegradation. We have observed that during light soaking shunts can develop, change in character, occasionally disappear. These changes are sometimes gradual, but often quite quick. It is not possible to predict when or whether a shunt will exist or develop. It is known that in general thin cells and modules are more susceptible to this problem but little concrete evidence exists due to the seemingly random appearance of these problems. The shunts which affect stability pass less current than those which lower the initial efficiency. While they can be measured by a dark I-V measurement, they have little or no impact on the initial efficiency of the cell or the module.

37

We have made considerable effort to locate shunts physically, hoping thereby to see the physical cause on the assumption that the shunt is a result of some kind of physical point defect or abnormality. To do so, small-area cells (0.25-cm^2) were laser scribed into 16 smaller cells, approximately 1-mm^2 each. It was found, when 0.25-cm^2 cells were subdivided into smaller cells, that there were groups of adjacent 1 mm^2 cells which were shunted and other groups of 1-mm^2 cells which were essentially shunt-free. An example of these patterns, extending across two 0.25-cm^2 cells is shown in **Figure 4.5**. However, while it was often possible to find suspicious features, it was rarely if ever possible to connect them to a shunt. Furthermore suspicious features found in 1-mm^2 diodes which were shunted could generally be found in their counterparts which were not shunted. Thus no distinct feature could be found to which the observed shunting behavior could be attributed. As we removed the layers by etching, first the metal, then a-Si, no specific defects peculiar to the shunted devices were unearthed. It may be that higher-power optical microscopy or electron microscopy could reveal small defects or differences in tin oxide morphology which could be associated with the shunted regions, however this would be a substantial and very painstaking effort which we have not yet undertaken. While it might be easy to find defects which could be tentatively linked to shunts, our experience is that it is hard to show that the same defects do not exist in shunt-free areas.

1	3	1	2
3	2	1	1
100	80	75	4
100	75	100	50

50	75	100	100
2	80	50	75
1	1	2	5
1	1	1	1

Figure 4.4 Two adjacent 0.25 cm^2 cells laser-scribed into two sets of 16 1-mm^2 cells. The numbers are the shunt current (in mA) passed in the dark at -2V. Larger numbers correspond to smaller shunt resistances. Shunted cells can be seen to be clustered together.
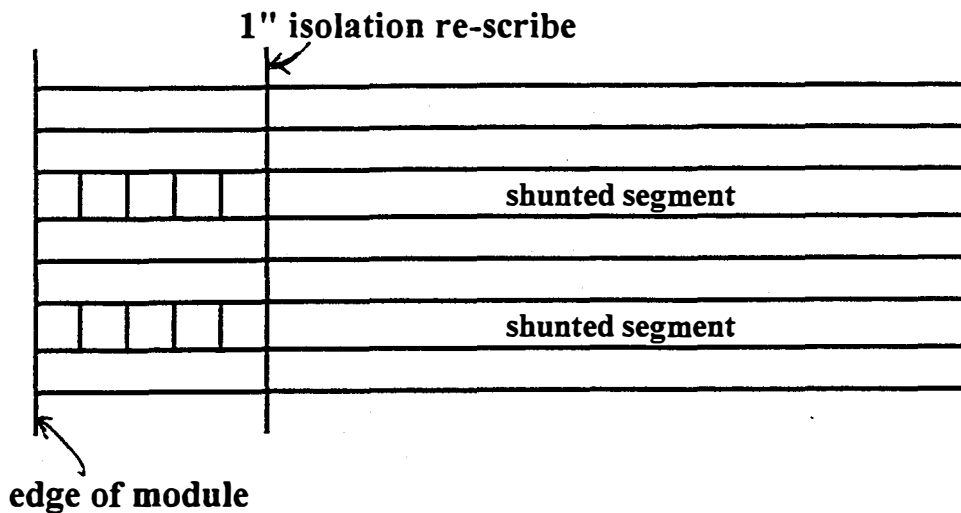
1" isolation re-scribe

shunted segment

shunted segment

edge of module

Figure 4.5 Shunted segments are identified before the 1-inch isolation re-scribe is done. If the re-scribe eliminates the shunts then the defect which caused the shunt must be located within the 1-inch length of segment at the module edge. By scribing this rejected region into smaller cells the position of the defect can be located even more finely.

4.7 Module and Device Modeling

In order to guide us in designing higher efficiency and more stable multi-junction a-Si:H based photovoltaic modules, we have developed a computer program to simulate multi-junction solar cell performance using the parameters of individual component junctions as input variables. The modeling software is based on a simple lump-circuit model which assumes perfect tunnel junctions or Ohmic contacts between the component cells in the monolithic stacked structure. Unlike any physical model such as AMPS developed at the Penn State University, our model is purely empirical and meant to explore the general behavior of the multi-junction devices without getting into the complicated, poorly understood underlying device physics and various material parameters. In this model, the I-V curve of each component cell is approximated by a Hecht expression based on the V_{oc}, J_{sc}, and FF of that cell. Then the I-V curve of the multi-junction device is computed from the I-V curves of the component cells under the constraint of current continuity. An additional series resistor can be introduced into the model circuit to reflect possible contact

39

resistance between the cells and front and/or back contact layers. The V_{oc}, J_{sc}, FF, and efficiency are obtained from the simulated I-V curve for the multi-junction cell. So far we have studied double-junction (tandem) and mostly triple-junction devices, however the simulation of higher number of junctions is also straightforward. Interestingly enough, data generated by this program have shown good, general agreement with our experimental data despite the simplicity of the model. In the following we briefly report on some findings and applications of this model. The next table shows an example of the triple-junction parameters derived from the component cell parameters. The predicted performance for the triple is in remarkable agreement with our data on high efficiency a-Si/a-Si/a-SiGe modules.

Table 4.3 Simulated triple-junction parameters and the input parameters of the component cells.

Device	*i*-layer	V_{oc} (V)	J_{sc} (mA/cm^2)	Fill Factor, FF	Efficiency, %
Top Junction	a-Si:H	0.92	6.75	0.73	4.53
Middle Junction	a-Si:H	0.9	6.75	0.69	4.19
Bottom Junction	a-SiGe:H	0.64	6.9	0.62	2.74
Triple	Si/Si/SiGe	2.46	6.77	0.687	11.4

Note that the J_{sc} of the triple (6.77 mA/cm^2) is slightly higher than the lowest J_{sc} of the component cells (6.75 mA/cm^2). This is because under the short-circuit condition, unless the J_{sc} is equal for each and every component cell, the internal voltages across the component cells are *not* zero due to the requirement of current continuity. The component cell with higher J_{sc} will be under a certain forward electrical bias while the component cell with lower J_{sc} will be under a certain reverse bias (so that the current flowing through each component cell is equal and the voltage across the two terminals of the stacked device is zero). As the result, the true J_{sc} of the triple can be slightly higher than the lowest J_{sc} of the component cells (which may be determined by, e.g., QE measurements). This result applies to stacked devices of any number of junctions.

Also note that, in the above table, the FF for the stacked device (0.687) is significantly higher than the lowest FF of the component cells, or the bottom a-SiGe junction (0.62). The same feature has been observed for a-Si/a-SiGe double-junction devices. The effect of current imbal-

ance on the FF of the multi-junction device has been extensively simulated using our model. The modeling indicates that current imbalance *always* improves the FF, and the more the imbalance, the bigger the improvement. In the case of large current imbalance, the FF for the triple device can be higher than that of the *highest* FF of the individual cells. In general, in agreement with our vast amount of experimental data, the stacked cell can exhibit much higher FF than one would expect from the relatively poor FF of the bottom a-SiGe junction, provided that the tunnel junction is adequately "Ohmic". In fact, this is true even when the a-SiGe junction is the current-limiting junction, in which case, intuitively, the poor FF of a-SiGe cell is expected to adversely impact the FF of the multi-junction device. Presently, a satisfactory explanation for this interesting and beneficial effect of "FF enhancement" is still lacking. With this knowledge, we can judge whether our experimental multi-junction modules have good tunnel junctions once we know the performance of the component junctions.

An important consideration for the initial and particularly the final efficiency of multi-junction solar cells is the match or mismatch of J_{sc} of the component cells. Significant insights have been gained using our lump-circuit model without making a large number of actual devices. Obviously, if all of the component cells have the same FF and degrade to the same extent under extended optical illumination, a perfect current match ($J_{sc1}=J_{sc2}=J_{sc3}$) will give the highest initial and final efficiency. However, in reality, the FF of any individual cell can be significantly lower than others, such as $i3$ in the Si/Si/SiGe triple. We have found that, in agreement with intuition, the highest performance is obtained under the condition of perfect current balance. Hence, the highest *final* efficiency is obtained when the *initial* J_{sc3} is slightly higher than the initial J_{sc1} and J_{sc2}. The overbalance of the initial J_{sc3} improves the *stabilized* efficiency because better current balance is obtained *after* light-degradation since the narrow-gap a-SiGe bottom cell loses more J_{sc} after light-soaking due to its poorer carrier collection efficiency and/or loss of optical reflectivity from the ZnO/Ag back contact. We have also found that the efficiency of the multijunction device can be made very close to the highest possible value even if there is moderate current mismatch (by up to, e.g., 0.3-0.4 mA/cm^2) among the component cells, since the reduction in J_{sc} can be largely compensated for by an increase in the FF due to the current mismatch. This also means that the efficiency of the multijunction devices can be reasonably well determined despite some deviation of the light source from the true spectral distribution of solar radiation which will cause different current imbalance from the component cells.

REFERENCES

[1] C.M. Fortmann, J. O'Dowd, J.L. Newton, AIP Conf. Proc. 157, Stability of Amorphous Silicon Alloy Materials and Devices, Palo Alto, California (1987), p. 103.

[2] M.S. Bennett, J.L. Newton, K. Rajan, Proceedings of the 7th E.C. P.V. Solar Energy Conf., Seville, (1986), p. 544.

[3] Y. Hamakawa, Y. Matsumoto, G. Hirata and H. Okamoto, MRS Symp. Proc. Vol. 164, 291 (1990); Y. Hattori, D. Kruangam, T. Toyama, H. Okamoto and Y. Hamakawa, Tech. Digest of 3rd Int'l Photovoltaic Science and Engineering Conf., Tokyo, Japan (1987) p. 171.

[4] S. Guha, J. Yang, P. Nath and M. Hack, Appl. Phys. Lett. 49, 218 (1986).

[5] T. Yoskida, K. Maruyama, O. Nabeta, Y. Ichikawa, H. Sakai and Y. Uchida, Proc. 19th IEEE Photovoltaic Specialist Conf., New Orleans (1987) p. 1095.

[6] R.R. Arya, et. al., Proceedings 23rd IEEE Photovoltaic Specialists Conference, Louisville, Kentucky, May (1993).

[7] See for example, Materials Issues in Microcrystalline Semiconductors, Eds. P.M. Fauchet, K. Tanaka, C.C. Tsai, MRS Symp. Proc. Vol. 164 (1990).

[8] R.W. Collins and B.Y. Yang, J. Vac, Sci. Technol. B7, 1155 (1989).

[9] M. Fang and B. Drevillon, J. Appl. Phys. 70, 4894 (1991).

[10] B. Goldsten, C.R. Dickson, I.H. Campbell and P.M. Fauchet, Appl. Phys. Lett. 53, 2672 (1988).

[11] J.Y. Hou, J.K. Arch, S.J. Fonash, S. Wiedeman and M. Bennett, Proc, 22nd IEEE Photovoltaic Specialist Conf., Las Vegas (1991) p. 1260

[12] M. Stutzman, W. Jackson, and C.C. Tsai, Phys. Rev. B32, 23 (1985).

[13] D. Redfield and R.H. Bube, Appl. Phys. Lett. 54, 1037 (1989).

[14] W.B. Jackson and J. Kakalios, Phys. Rev. B 37, 1020 (1988).

[15] W.B. Jackson, in *Amorphous silicon Technology-1989*, MRS Symp. Proc. Vol. 149 (Materials Research Society, Pittsburgh, 1989), p. 571

[16] R.S. Crandell, Phys. Rev. B 43, 4057 (1991).

[17] D. Redfield, in *Amorphous silicon Technology-1992*, MRS Symp. Proc. Vol. 258 (Materials Research Society, Pittsburgh, 1992), p. 341.

[18] L. Yang, L. Chen and A. Catalano, April, Phys. Lett. 59, 840 (1991).

[19] M.S. Bennett, J.L. Newton, K. Rajan and A. Rothwarf, J. Appl. Phys. 62, 3968 (1987).

[20] T.J. McMahon, in *Amorphous silicon Technology-1992*, MRS Symp. Proc. Vol. 258 (Materials Research Society, Pittsburgh, 1992), p. 325.

[21] D. Fischer, N. Pellaton, H. Keppner, A. Shah, C.M. Fortmann, in *Amorphous silicon Technology-1992*, MRS Symp. Proc. Vol. 258 (Materials Research Society, Pittsburgh, 1992), p. 893.

[22] L. Chen and L. Yang, J. Non-Crystalline Solids 137 & 138, 1185 (1991).

[23] Z. Smith, S. Wagner, and B.W. Faughnan, Appl. Phys. Lett. 46, 1078 (1985).

[24] M. Bennett K. Rajan, K. Kritikson, to be published in Proc. of 23rd IEEE Photovoltaic Specialists Conf., Louisville, Kentucky, 1993.

[25] L. Yang, *et al.*, to be published.

[26] Research on Stable, High Efficiency, Amorphous Silicon Multijunction Modules, Annual Report, July 1992, (contract #ZM-0-19033-1), Solarex Corporation, Thin-Film Division

[27] J. Morris, R. Arya, J. O'Dowd and S. Wiedeman; J. Appl. Physics, 67, 1079 (1990)

[28] S. Wiedeman, J. Morris and L. Yang, Proceedings 21st IEEE Photovoltaic Specialists Conference, (1990).

REPORT DOCUMENTATION PAGE

1. AGENCY USE ONLY (Leave blank)	2. REPORT DATE June 1994	3. REPORT TYPE AND DATES COVERED Final Subcontract Report - 1 July 1992 - 30 June 1993

4. TITLE AND SUBTITLE

Research on Stable, High-Efficiency, Amorphous Silicon Multijunction Modules

5. FUNDING NUMBERS

C: ZM-0-19033-1

TA: PV431101

6. AUTHOR(S)

R.R. Arya, M. Bennett, L. Chen, B. Fieselmann, Y. Li, N. Maley, J. Newton, R. Podlesny, L. Yang

7. PERFORMING ORGANIZATION NAME(S) AND ADDRESS(ES)

Solarex Thin Film Division
826 Newtown-Yardley Road
Newtown, PA 18940

8. PERFORMING ORGANIZATION REPORT NUMBER

9. SPONSORING/MONITORING AGENCY NAME(S) AND ADDRESS(ES)

National Renewable Energy Laboratory
1617 Cole Blvd.
Golden, CO 80401-3393

10. SPONSORING/MONITORING AGENCY REPORT NUMBER

TP-411-6841

DE94011826

11. SUPPLEMENTARY NOTES

NREL Technical Monitor: W. Luft

12a. DISTRIBUTION/AVAILABILITY STATEMENT

12b. DISTRIBUTION CODE

UC-271

13. ABSTRACT (Maximum 200 words)

This report describes work performed during the period 1 July 1992 through 30 June 1993. During this period, major improvements were achieved in the stabilized conversion efficiency of triple-junction modules. These resulted in the demonstration of triple-junction initial conversion efficiency of 11.3% and stabilized conversion efficiency of approximately 9%. Significant advances were made in the deposition of a-Si:H intrinsic layers that led to higher open-circuit voltage and improved stability. Thin microcrystalline n-layers were developed and scaled up for the recombination junctions in triple-junction modules that resulted in higher open-circuit voltage and fill factors. These improvements resulted in the demonstration of a-Si/a-Si/a-SiGe triple-junction modules with initial conversion efficiencies as high as 11.35% and "stabilized" efficiencies of about 9%.

14. SUBJECT TERMS

high efficiency ; amorphous silicon ; modules ; photovoltaics ; solar cells

15. NUMBER OF PAGES
56

16. PRICE CODE
A04

17. SECURITY CLASSIFICATION OF REPORT Unclassified	18. SECURITY CLASSIFICATION OF THIS PAGE Unclassified	19. SECURITY CLASSIFICATION OF ABSTRACT Unclassified	20. LIMITATION OF ABSTRACT UL